

Massive gauge boson pair production at the LHC: a next-to-leading order story

Julien Baglio¹, Le Duc Ninh^{1,2} and Marcus M. Weber³

¹ Institut für Theoretische Physik, Karlsruher Institut für Technologie,
Wolfgang Gaede Straße 1, Karlsruhe DE-76131, Germany

² Institute of Physics, Vietnam Academy of Science and Technology,
10 Dao Tan, Ba Dinh, Hanoi, Vietnam

³ Max-Planck-Institut für Physik (Werner-Heisenberg-Institut),
D-80805 München, Germany

Abstract

Electroweak gauge boson pair production is one of the most important Standard Model processes at the LHC, not only because it is a benchmark process but also by its ability to probe the electroweak interaction directly. We present full next-to-leading order predictions for the production cross sections and distributions of on-shell massive gauge boson pair production in the Standard Model. This includes the QCD and electroweak corrections. We study the hierarchy between the different channels when looking at the size of the QCD gluon-quark induced processes and the electroweak photon-quark induced processes and provide the first comprehensive explanation of this hierarchy thanks to analytical leading-logarithmic results. We also provide a detailed study of the theoretical uncertainties affecting the total cross section predictions that stem from scale variation, parton distribution function and α_s errors. We then compare with the present LHC data.

1 Introduction

Since the start of LHC operations in 2010 there have been already several measurements involving electroweak (EW) gauge bosons, e.g. the standard candles W and Z production cross sections [1–4]. In addition to these standard measurements, the gauge boson pair production mechanisms provide a very important test of the Standard Model (SM) structure as it is a way to probe directly the non-abelian structure of EW symmetry and in particular the trilinear couplings among the W , γ and Z bosons. Physics beyond the SM may hide in anomalous couplings and could be visible in gauge boson pair production at the LHC. The ATLAS and CMS Collaborations have already provided measurements and limits on these anomalous gauge boson couplings [5–11]. In addition, WW and ZZ production are amongst the most important irreducible backgrounds in Higgs boson studies, see Ref. [12] for example. This leads to the requirement of precise experimental measurements on the one side and rigorous theoretical understanding on the other side.

The QCD next-to-leading order (NLO) corrections to gauge boson pair production have been known for a long time [13–18], both for the total cross sections and the differential distributions, including the decays of the produced gauge bosons [19, 20]. A full next-to-next-to-leading order (NNLO) QCD calculation is still missing even if partial NNLO results have been obtained recently, see e.g. Ref. [21] for WZ channel and Ref. [22] for WW channel. Next-to-next-to-leading logarithmic calculations are also available for WW production [23]. As for EW corrections, they have been known for long only in the high energy approximation [24–26] and only very recently the full NLO EW corrections have been calculated for diboson production [27–29], with the notable exception of photon-quark induced processes.

The goal of this paper is to provide full NLO calculations for the on-shell WW , WZ and ZZ cross sections at the LHC, with both EW and QCD effects. In particular the EW corrections include photon-quark initial-state processes that have not yet been considered in the literature. WW and ZZ cross section calculations also include the well-known gluon fusion subprocess [30–35] that is formally a NNLO contribution. Furthermore we include the photon-photon induced process in the WW cross section calculation. The LO contribution to this photon-photon induced process has been studied in Ref. [27]. We also present some distributions for the three different processes, without any cuts, to study the effect of the separate contributions to the NLO corrections, especially at high p_T . In particular we present a detailed analysis of the hierarchy that is observed in the size of the QCD gluon-quark induced corrections and the EW photon-quark induced corrections. We provide the first comprehensive explanation of the large differences seen in ZZ , WZ and WW channels. There have been attempts to explain them in the case of QCD gluon-quark induced corrections [14, 15, 19]. However, to our best knowledge, it has not been understood why the WW channel is so different from the ZZ channel [19]. We will show that the differences are essentially due to non-abelian gauge structure of the SM, different coupling strengths and parton distribution function (PDF) effects. Our explanation differs from the one given in Refs. [14, 15, 19]. We will also show that including the photon-quark induced processes is important in the case of the EW corrections to WZ and WW channels, compensating or even overcompensating the virtual EW Sudakov effect. In order to compare with experimental data, we also perform a detailed analysis of the different sources of uncertainties that affect the theoretical calculation of the total cross section. This includes the scale uncertainty that stems from the variation of the renormalization and the factorization

scales, providing an estimate of the missing higher-order corrections; the uncertainty related to the parton distribution function (PDF) and the associated error on the determination of the strong coupling constant α_s . The uncertainties related to the experimental errors on the W and Z masses are found to be negligible. We also study the interplay between single-top and WW production modes and find that the interference effects are negligible.

The paper is organized in the following way: in a first section we present the ingredients of the calculation and in particular the calculation of the full EW corrections. We then move to the numerical analysis and present the setup as well as the distributions for the different processes, using analytical calculations to explain the hierarchy in the QCD and EW corrections between WW , WZ and ZZ mechanisms. In a third section we carry out the analysis of the theoretical uncertainties on the total cross section. We also compare with ATLAS and CMS results. A short conclusion will then be given. The reader will also find an appendix where the details of the analytical approximation of the photon-quark induced process in W^+Z channel are given as an example.

2 Computational details

We consider in this paper the production of two on-shell massive gauge bosons at the LHC. The contributions from the third-generation quarks in the initial state are excluded (see the discussion on the b -quark contribution in Section 3.6) unless otherwise stated. The main mechanism to produce two massive gauge bosons is therefore via quark anti-quark annihilations as shown in Fig. 1a. The special $\gamma\gamma \rightarrow W^+W^-$ reaction, which occurs at tree level and includes the quartic $\gamma\gamma W^+W^-$ coupling as depicted in Fig. 1b, is also taken into account. Even though this contribution is very small at the total cross section level, it increases with the invariant mass M_{WW} and is comparable with opposite sign to the leading EW corrections for the invariant mass distribution, as shown in Section 3.4. For the case of W^+W^- and ZZ , the subdominant one-loop gluon fusion processes, as displayed in Fig. 2 and which are formally NNLO contributions, are also included in our calculation. These corrections have been calculated in Refs. [30–35]. We re-calculate them here for the sake of completeness. The leading order (LO)

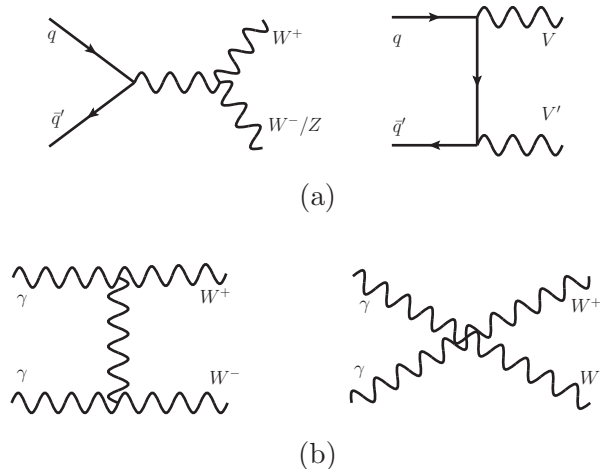


Figure 1: Representative tree-level diagrams for VV' production processes.

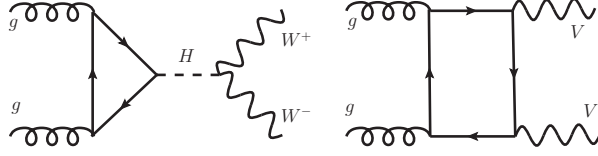


Figure 2: Representative diagrams for VV' production via gluon-gluon fusion.

hadronic cross section is defined as

$$\sigma_{\text{LO}} = \int dx_1 dx_2 [\bar{q}_{\text{LO}}(x_1, \mu_F) q'_{\text{LO}}(x_2, \mu_F) \hat{\sigma}_{\text{LO}}^{\bar{q}q' \rightarrow VV'} + (1 \leftrightarrow 2)], \quad (1)$$

where q and \bar{q} are the parton distribution functions (PDF) of the first and second generation quarks in the proton at the momentum fraction x and factorization scale μ_F , and $\hat{\sigma}^{\bar{q}q' \rightarrow VV'}$ the LO partonic cross section. The photon-photon and gluon-gluon contributions read

$$\begin{aligned} \sigma_{\text{LO}}^{\gamma\gamma} &= \int dx_1 dx_2 [\gamma_{\text{LO}}(x_1, \mu_F) \gamma_{\text{LO}}(x_2, \mu_F) \hat{\sigma}_{\text{LO}}^{\gamma\gamma \rightarrow VV'}], \\ \sigma^{gg} &= \int dx_1 dx_2 [g(x_1, \mu_F) g(x_2, \mu_F) \hat{\sigma}^{gg \rightarrow VV'}], \end{aligned} \quad (2)$$

and are understood as corrections over the LO hadronic cross section of Eq. (1).

In the following, we sketch the main points of our NLO calculation. We will define various sub-corrections at NLO, namely the QCD virtual, gluon-quark radiated and gluon-quark induced corrections for the QCD case and the EW virtual, photon-quark radiated and photon-quark induced corrections for the EW case. These sub-corrections are ultraviolet (UV) and infrared (IR) finite, but are dependent on the regularization scheme. The final results, *i.e.* the sum of those sub-corrections, are of course regularization-scheme independent. The separation will help to better understand the QCD and EW corrections.

2.1 NLO QCD corrections

The NLO QCD contribution includes the loop corrections with one gluon in the loops and the real emission corrections with one additional parton in the final state. We classify the real emission contribution into two groups: gluon-quark radiated processes $\bar{q}q' \rightarrow VV'g$, where the gluon is radiated from an initial (anti-)quark and gluon-quark induced processes $qg \rightarrow VV'q'$, which are related to the gluon-quark radiated ones via crossing symmetry. Both the virtual and real corrections are separately IR divergent. These divergences cancel in the sum for infrared-safe observables such as the total cross section and kinematic distributions of massive gauge bosons. The dimensional regularization (DR) method [36] is used to regularize the infrared divergences unless otherwise stated. Moreover, we apply the Catani-Seymour dipole subtraction algorithm [37] to combine the virtual and the real contributions. We use the same notations as in Ref. [37] and define the various NLO QCD corrections as follows,

$$\begin{aligned} \sigma_{\text{QCD-virt}} &= \int dx_1 dx_2 [\bar{q}_{\text{NLO}}(x_1, \mu_F) q'_{\text{NLO}}(x_2, \mu_F) \hat{\sigma}_{\text{QCD-virt}}^{\bar{q}q' \rightarrow VV'} + (1 \leftrightarrow 2)], \\ \hat{\sigma}_{\text{QCD-virt}}^{\bar{q}q' \rightarrow VV'} &= \hat{\sigma}_{\text{QCD-loop}}^{\bar{q}q' \rightarrow VV'} + \hat{\sigma}_{\text{QCD-I}}^{\bar{q}q' \rightarrow VV'}, \end{aligned} \quad (3)$$

where $\hat{\sigma}_{\text{QCD-loop}}^{\bar{q}q' \rightarrow VV'}$ includes only loop diagrams and $\hat{\sigma}_{\text{QCD-I}}^{\bar{q}q' \rightarrow VV'}$ is the I-operator contribution as defined in Ref. [37]. It is noted that $\hat{\sigma}_{\text{QCD-virt}}^{\bar{q}q' \rightarrow VV'}$ is UV and IR finite. The gluon-quark radiated and gluon-quark induced contributions read

$$\begin{aligned}\sigma_{\text{g-rad}} &= \int dx_1 dx_2 [\bar{q}_{\text{NLO}}(x_1, \mu_F) q'_{\text{NLO}}(x_2, \mu_F) (\hat{\sigma}^{\bar{q}q' \rightarrow VV'g} - \hat{\sigma}_{\text{QCD-I}}^{\bar{q}q' \rightarrow VV'}) + (1 \leftrightarrow 2)], \\ \sigma_{\text{g-ind}} &= \int dx_1 dx_2 [q_{\text{NLO}}(x_1, \mu_F) g_{\text{NLO}}(x_2, \mu_F) \hat{\sigma}^{qg \rightarrow VV'q'} + (1 \leftrightarrow 2)].\end{aligned}\quad (4)$$

These contributions are also IR finite because the collinear divergences occurring at the partonic level are absorbed into the quark PDFs.

2.2 NLO EW corrections

The NLO EW corrections are also divided into similar sub-contributions as in the QCD case, but there are some important differences. The loop corrections contain UV divergences. They are regularized using the DR method [36, 38] and by the renormalization of the relevant EW parameters, namely M_W , M_Z and the fine-structure constant α . The presence of fermion loops with γ_5 , as shown in Fig. 3, requires that all lepton and quark contributions must be included to cancel the anomaly. For the process $\gamma\gamma \rightarrow W^+W^-$ we use the on-shell scheme (see e.g.

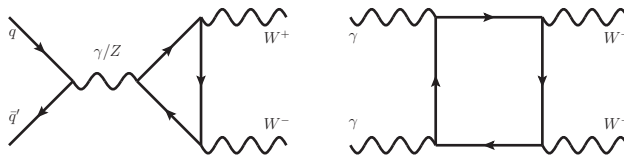


Figure 3: Selected fermion-loop diagrams with γ_5 .

Ref. [39]) where $\alpha(q^2)$ is defined in the Thomson limit at $q^2 \rightarrow 0$. This is justified because the LO amplitudes involve real photons, hence the running of α is absent. We note that the virtual and soft-photon corrections to this process have been calculated in Ref. [40]. For $\bar{q}q' \rightarrow VV'$ processes, using $\alpha(0)$ as an input parameter induces large corrections of the form $\log(Q^2/m_f^2)$ with Q being a typical hard energy scale and m_f the light fermion masses in the loop contribution. Those corrections can be absorbed into the running of α using $\alpha(M_Z^2)$ or using the G_μ -scheme with $\alpha_{G_\mu} = \sqrt{2}G_\mu M_W^2(1 - M_W^2/M_Z^2)/\pi$ as an input parameter. We choose the latter and hence the calculation is consistently done by fixing the renormalization constant of the electric charge as

$$\delta Z_e^{G_\mu} = \delta Z_e^{\alpha(0)} - \frac{1}{2}(\Delta r)_{1\text{-loop}},\quad (5)$$

where $(\Delta r)_{1\text{-loop}}$ is defined in [41, 42]. An advantage of this framework is that the final results are independent of the light fermion masses. The above discussion also makes it clear that one should use the coupling $\alpha(0)$ for vertices with a real photon directly attached to them. Therefore, the NLO EW corrections to $\bar{q}q' \rightarrow VV'$ processes are proportional to $\alpha_{G_\mu}^2 \alpha(0)$, while it is $\alpha(0)^3$ for $\gamma\gamma \rightarrow W^+W^-$. We now take into account the real corrections and combine them

with the virtual ones using the notation of Ref. [43]. We use by default the mass regularization (MR) method, *i.e.* introducing a common mass regulator for the light fermions (all but the top quark) and a fictitious photon mass, to regularize IR divergences. For $\gamma\gamma \rightarrow W^+W^-$ process, we have

$$\begin{aligned}\sigma_{\text{NLO}}^{\gamma\gamma} &= \int dx_1 dx_2 [\gamma_{\text{NLO}}(x_1, \mu_F) \gamma_{\text{NLO}}(x_2, \mu_F) \hat{\sigma}_{\text{NLO}}^{\gamma\gamma \rightarrow VV'}], \\ \hat{\sigma}_{\text{NLO}}^{\gamma\gamma \rightarrow VV'} &= \hat{\sigma}_{\text{LO}}^{\gamma\gamma \rightarrow VV'} + \hat{\sigma}_{\text{EW-loop}}^{\gamma\gamma \rightarrow VV'} + \hat{\sigma}^{\gamma\gamma \rightarrow VV'\gamma}.\end{aligned}\quad (6)$$

For the $\bar{q}q' \rightarrow VV'$ processes, the correction $\sigma_{\text{EW-virt}}$ is, similarly to the QCD case, given as in Eq. (3), but the I-operator contribution $\hat{\sigma}_{\text{EW-I}}^{\bar{q}q' \rightarrow VV'}$ is now defined as the endpoint contribution of Ref. [43]. The photon-quark radiated and photon-quark induced contributions read

$$\begin{aligned}\sigma_{\gamma\text{-rad}} &= \int dx_1 dx_2 [\bar{q}_{\text{NLO}}(x_1, \mu_F) q'_{\text{NLO}}(x_2, \mu_F) (\hat{\sigma}^{\bar{q}q' \rightarrow VV'\gamma} - \hat{\sigma}_{\text{EW-I}}^{\bar{q}q' \rightarrow VV'}) + (1 \leftrightarrow 2)], \\ \sigma_{\gamma\text{-ind}} &= \int dx_1 dx_2 [q_{\text{NLO}}(x_1, \mu_F) \gamma_{\text{NLO}}(x_2, \mu_F) \hat{\sigma}^{q\gamma \rightarrow VV'q'} + (1 \leftrightarrow 2)].\end{aligned}\quad (7)$$

For EW corrections, we use $f_{\text{NLO}}(x, \mu_F) = f_{\text{LO}}(x, \mu_F)$ for $f = q, \bar{q}, \gamma$ as given by the current only PDF set that exists including the photon PDF¹, namely MRST2004QED [45]. Moreover, the collinear divergences occurring at the partonic level in the photon-quark radiated and photon-quark induced contributions are absorbed into the (anti-)quark and photon PDFs using the DIS factorization scheme as done in Ref. [46]. We note that the virtual and photon-quark radiated contributions have been calculated in Refs. [27–29], but the photon-quark induced processes were not considered and the $\gamma\gamma$ contribution was considered at LO only.

In addition to the MR scheme, we have also implemented the DR scheme to deal with IR divergences for $\bar{q}q' \rightarrow VV'$ processes. For QCD corrections the DR method is explained in detail in Ref. [47]. For EW corrections the same procedure holds. This is because, as in the QCD case, the rational terms of the IR origin come only from the collinear single pole in the wave-function corrections of massless particles. The soft divergences related to the $W^+W^-\gamma$ vertex do not introduce any rational term. Moreover, by using the α_{G_μ} scheme, the results are independent of the light fermion masses. These masses can therefore be set to zero. We have checked that, by using the same subtraction term in the $2 \rightarrow 3$ contribution, the sum of the I-operator and the PK-operator (as defined in Ref. [37] for DR and being the convolution part in Ref. [43] for MR) contributions is in agreement within statistical errors for the MR and the DR methods.

The aforementioned method has been implemented in different computer codes, using FORTRAN77 and C++ programming languages. The helicity amplitudes are generated using FeynArts-3.4 [48] and FormCalc-6.0 [49] as well as HELAS [50, 51]. The scalar and tensor one-loop integrals are evaluated with the in-house library LoopInts, which agrees with LoopTools program [49, 52]. In these codes, the tensor integrals are recursively reduced to scalar integrals using the Passarino-Veltman algorithm [53] and the scalar integrals are calculated as in Refs. [54–57]. Moreover, the real corrections have been checked by comparing the results of the dipole-subtraction method with those of the phase-space slicing method [58].

¹The NNPDF Collaboration has recently started a QED study of parton functions [44]. A new QED PDF has just been released in the LHAPDF framework.

3 Differential cross sections

3.1 Parameter setup

Our default set of input parameters is

$$\begin{aligned} G_\mu &= 1.16637 \times 10^{-5} \text{ GeV}^{-2}, M_W = 80.385 \text{ GeV}, M_Z = 91.1876 \text{ GeV}, \\ M_t &= 173.5 \text{ GeV}, M_H = 125 \text{ GeV}, \end{aligned} \tag{8}$$

taken from Refs. [59–61]. The CKM matrix is assumed to be diagonal. The effect is at most -0.7% (-1%) on the total $W^+Z(W^-Z)$ cross section. The masses of the leptons and the light quarks, *i.e.* all but the top mass, are approximated as zero. This is justified because our results are insensitive to those small masses. As argued in Section 2.2, the NLO EW corrections to $\bar{q}q' \rightarrow VV'$ processes are proportional to $\alpha_{G_\mu}^2 \alpha(0)$ where $\alpha_{G_\mu} = \sqrt{2}G_\mu M_W^2(1 - M_W^2/M_Z^2)/\pi$ (which can be understood as $\alpha(M_W^2)$) and $\alpha(0) = 1/137.036$ is used as an input parameter. This is because the relation $\alpha_{G_\mu} = \alpha(0)(1 + \Delta r)$ depending on the hadronic contribution to the photon self-energy at low energy is not reliable and hence we do not use it to calculate $\alpha(0)$. We only list in this section the central values for the parameters, the uncertainties that affect them will be described in Section 4. For the MRST2004QED set of PDFs we use $\alpha_s^{\text{NLO}}(M_Z^2) = 0.1190$ and the NLO running with five flavors for all subprocesses. When switching to modern PDF sets such as MSTW2008 [62], the difference is $\alpha_s^{\text{NLO}}(M_Z^2) = 0.12018$ and $\alpha_s^{\text{NNLO}}(M_Z^2) = 0.11707$ (in this example). The NNLO value (and running) of the strong coupling constant is used for $gg \rightarrow W^+W^-, ZZ$ subprocesses. Otherwise the strong coupling constant gets its NLO value and the running is also evaluated at NLO. We also define the following central scale for the process $pp \rightarrow VV'$,

$$\mu_R = \mu_F = \mu_0 = M_V + M_{V'}. \tag{9}$$

This choice is justified because, as we will see, the bulk of the total cross section comes from the low energy regime. In the following, we will study the distributions using only the MRST2004QED PDF set. We apply no cuts at the level of the W^\pm and Z , since these will decay. Analytical results for leading-logarithmic corrections arising from the QCD gluon-quark induced processes and the EW photon-quark induced processes will also be presented. Their proofs are given in the Appendix.

3.2 ZZ distributions

We start the discussion of the distributions with the ZZ process. In this subsection and the following we display the transverse momentum of one of the gauge bosons, the invariant mass and the rapidity distributions of the gauge boson pair. The considered center-of-mass (c.m.) energy will be $\sqrt{s} = 14 \text{ TeV}$. We use $\Delta K_X = d\sigma_X/d\sigma_{\text{LO}}$ to describe the various corrections when $\Delta K_{\text{NLO}} > 1$, otherwise we will discuss in terms of percentage corrections. We use the MRST2004QED PDF set both at LO and NLO.

The first distributions that we display in Fig. 4 are the transverse momentum p_T^Z of one Z boson as well as the differential distribution of the invariant mass M_{ZZ} of the Z boson pair, calculated at LO and NLO including QCD and EW corrections. In practice, since the two Z

bosons in the final state are identical, the binning of the p_T^Z histogram is done by selecting both particles and rescaling the final result by symmetry factor 1/2. The gg contribution is also separately shown.

To analyze in more details we display in Fig. 5 and Fig. 6 the p_T^Z and M_{ZZ} distributions of the QCD and EW corrections, relative to the LO $q\bar{q}$ results, for the various sub-corrections defined in Section 2. For the p_T^Z distributions, the QCD corrections have the expected behavior known from the previous studies [14, 15], namely $qg \rightarrow ZZq$ processes dominate entirely the NLO QCD corrections of the $q\bar{q}$ subprocesses, up to $\Delta K = 1.5$ at $p_T^Z = 700$ GeV. It is important to note that the $d\bar{d}$ contribution is about 1.3 times larger than the $u\bar{u}$ one for a large range of p_T^Z about 700 GeV at LO because of larger couplings, while the $dg \rightarrow ZZd$ and $ug \rightarrow ZZu$ contributions are about the same. The $\bar{q}g \rightarrow ZZ\bar{q}$ processes are much smaller. This large correction can be explained as follows. At large p_T^Z , both Z bosons are hard with the same transverse momentum at LO. For the process $qg \rightarrow ZZq$, the dominant mechanism is first to produce one Z and a quark with large transverse momentum, and then the hard quark radiates a soft Z . For $p_T^Z \gg M_Z$ we have, see the Appendix for more details,

$$\begin{aligned} \frac{d\sigma^{qg \rightarrow ZZq}}{d\sigma_{\text{LO}}^{\bar{q}q \rightarrow ZZ}} &= \frac{c_{L,q}^2 d\sigma_L^{qg \rightarrow Zq} + c_{R,q}^2 d\sigma_R^{qg \rightarrow Zq}}{4d\sigma_{\text{LO}}^{\bar{q}q \rightarrow ZZ}} \frac{\alpha}{2\pi} \log^2 \left[\frac{(p_T^Z)^2}{M_Z^2} \right] \\ &= c_{ZZ}^q \frac{d\sigma_L^{qg \rightarrow Zq}}{d\sigma_{\text{LO}}^{\bar{q}q \rightarrow ZZ}} \frac{\alpha}{2\pi} \log^2 \left[\frac{(p_T^Z)^2}{M_Z^2} \right], \end{aligned} \quad (10)$$

where $c_{L,f} = (I_3^f - \sin^2 \theta_W Q_f)/(\sin \theta_W \cos \theta_W)$ and $c_{R,f} = -Q_f \sin \theta_W / \cos \theta_W$ with $I_3^f = \pm 1/2$ being the third component of the weak isospin and Q_f being the electric charge of the fermion f , and $c_{ZZ}^q = (c_{L,q}^4 + c_{R,q}^4)/(4c_{L,q}^2)$ about 0.18 for up quarks and 0.26 for down quarks. A sum over u and d flavors is implicitly assumed in Eq. (10). At $p_T = 700$ GeV we have

$$\frac{\alpha}{2\pi} \log^2 \left[\frac{(p_T)^2}{M_Z^2} \right] \approx 0.020, \quad \frac{\alpha}{2\pi} \log^2 \left[\frac{(p_T)^2}{M_W^2} \right] \approx 0.023. \quad (11)$$

The first ratio on the right-hand side of Eq. (10) is large because the denominator is an EW process while the numerator is proportional to $\alpha_s(\mu_0)$ and involves the large gluon PDF. Numerically, we get $\Delta K_{qg} = 1.51$ (1.20) for leading-logarithmic approximation (full calculation) at $p_T^Z = 700$ GeV.

In the invariant mass distribution the gluon-quark induced and the gluon-quark radiated processes compensate each other and the full QCD corrections are dominated by the virtual corrections. The gluon fusion mechanism amounts to $\sim +10\%$ in the M_{ZZ} distribution and is negligible in the transverse momentum distribution.

Turning to EW corrections in Fig. 6, we observe that the effect of the virtual Sudakov logarithms $\alpha \log^2[(p_T^Z)^2/M_W^2]$ is clearly visible in Fig. 6 (left) where the dotted red curve is the p_T^Z distribution of the virtual EW corrections, and we have for example a -40% correction at $p_T^Z = 700$ GeV. The photon-quark induced processes have similar behaviors as the gluon-quark induced processes, except that there are now the photon PDF and the EW $\alpha(0)$ coupling, instead of the gluon PDF and α_s , in the right-hand side of Eq. (10). For $p_T^Z \gg M_Z$ we have

$$d\sigma^{q\gamma \rightarrow ZZq} = c_{ZZ}^q d\sigma_L^{q\gamma \rightarrow Zq} \frac{\alpha}{2\pi} \log^2 \left[\frac{(p_T^Z)^2}{M_Z^2} \right]. \quad (12)$$

This explains why the correction is negligible. Numerically, we get 0.3% (0.3%) for leading-logarithmic approximation (full calculation) at $p_T^Z = 700$ GeV. The same effect is visible in the invariant mass distribution, where the total EW corrections are dominated by the virtual EW contribution and drop to -8% at $M_{ZZ} = 700$ GeV.

We also display the rapidity distribution of the Z pair in Fig. 7, that gives the trend of $\log(x_1/x_2)$ momentum fraction of the incoming partons. The impact of the gluon fusion channel is much smaller than the NLO QCD corrections on $q\bar{q}$ sub-channels as seen in the upper left panel. The latter corrections amount to a $\sim +26\%$ increase. The upper right panel of Fig. 7 displays the rapidity distribution of the EW corrections and the same effect seen in the transverse momentum and invariant mass distributions is clearly visible: the photon-quark induced and photon radiated processes do not contribute at all and all the EW corrections are driven by the virtual corrections. The shape is then quadratic with a flat minimum of $\sim -4\%$ for $|y_{ZZ}| \leq 3.5$. This result is consistent with the one of Ref. [29].

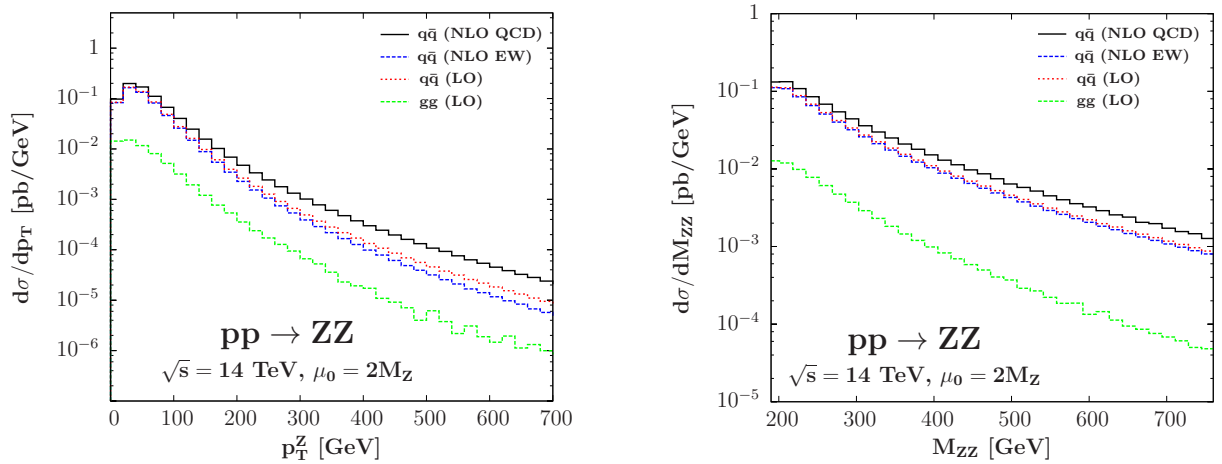


Figure 4: Z transverse momentum p_T (in GeV) distribution (left) and Z pair invariant mass M_{ZZ} (in GeV) distribution (right) of $pp \rightarrow ZZ$ cross section at the LHC (in pb/GeV), including NLO QCD and EW corrections calculated with MRST2004QED PDF set and with the input parameters described in Section 3.1. In the M_{ZZ} distribution the $q\bar{q}$ LO (dotted red) and $q\bar{q}$ NLO EW (dashed blue) curves nearly coincide.

3.3 WZ distributions

We now present the same distributions as above but for the W^+Z and W^-Z channels. We start with the transverse momentum distributions of the W^\pm boson and of the Z boson displayed in Fig. 8, including NLO QCD and EW corrections. Both W^+Z and W^-Z channels are depicted and one can see the same trend in both channels for both W^\pm and Z transverse momenta. The main difference between W^+Z and W^-Z channels comes from the EW corrections at high transverse momentum: in the first case there are basically no EW corrections (upper panels) while in the latter case the EW corrections increase the differential cross section by a limited amount (lower panels).

In the case of the NLO QCD corrections we observe the expected behavior with similar shape for both distributions in W^+Z and W^-Z channels, as displayed in Fig. 9. The QCD corrections are up to $\Delta K \sim 7$ at $p_T^{W^+} \sim 700$ GeV and $p_T^Z \sim 700$ GeV in the W^+Z channel and

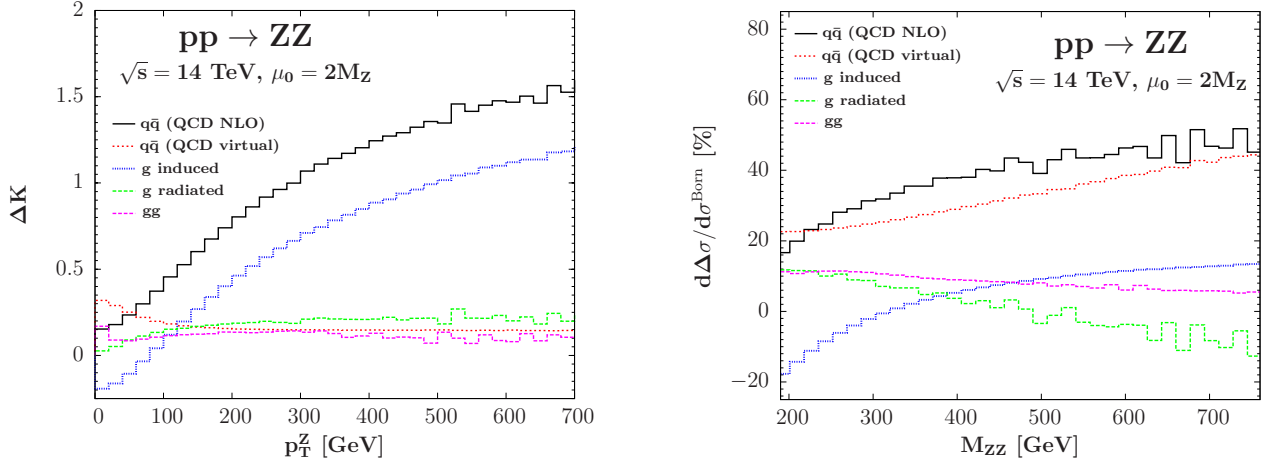


Figure 5: Z transverse momentum p_T (in TeV) distribution (left, using ΔK) and Z pair invariant mass M_{ZZ} (in GeV) distribution (right, in %) of the NLO QCD corrections to $pp \rightarrow ZZ$ cross section at the LHC, calculated with MRST2004QED PDF set and with the input parameters described in Section 3.1.

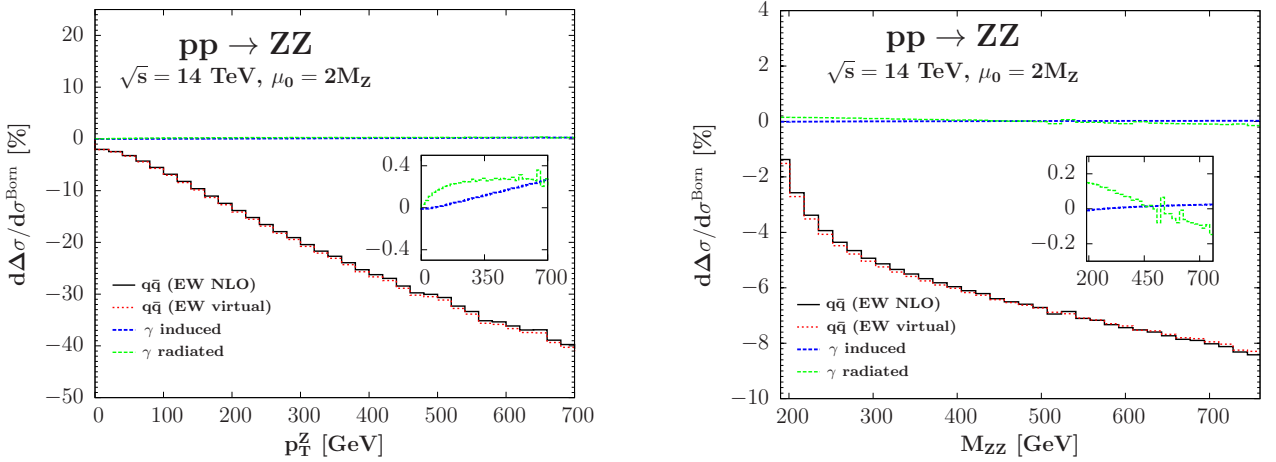


Figure 6: Same as Fig. 5 but for EW corrections (in %). The $q\bar{q}$ EW NLO and $q\bar{q}$ EW virtual curves nearly coincide as well as the photon-quark induced and photon radiated curves.

larger in the W^-Z channel with corrections up to $\Delta K \sim 8$ at $p_T^{W^-} \sim 700$ GeV and $\Delta K \sim 9$ at $p_T^Z \sim 700$ GeV. Similar to the ZZ case, those huge corrections can be explained as follows. For the $p_T^{W^+}$ distribution the dominant mechanism is $ug \rightarrow W^+d$ and then a soft Z is radiated from a quark or the W^+ . For $p_T^{W^+} \gg M_Z$ we have, with $a_W = 1/(\sqrt{2} \sin \theta_W)$,

$$\begin{aligned}
 d\sigma^{ug \rightarrow W^+Zd} &= \frac{1}{2} c_{L,d} c_{L,u} \left(1 + \frac{\cot \theta_W}{c_{L,d}} - \frac{\cot \theta_W}{c_{L,u}} \right) d\sigma_L^{ug \rightarrow W^+d} \frac{\alpha}{2\pi} \log^2 \left[\frac{(p_T^{W^+})^2}{M_Z^2} \right] \\
 &= c_{WZ}^u d\sigma_L^{ug \rightarrow Zu} \frac{\alpha}{2\pi} \log^2 \left[\frac{(p_T^{W^+})^2}{M_Z^2} \right], \\
 c_{WZ}^u &= \frac{1}{2} a_W^2 \frac{c_{L,d}}{c_{L,u}} \left(1 + \frac{\cot \theta_W}{c_{L,d}} - \frac{\cot \theta_W}{c_{L,u}} \right) = 4.13,
 \end{aligned} \tag{13}$$

where the $\bar{d}g$ contribution, about an order of magnitude smaller than the ug one, has been

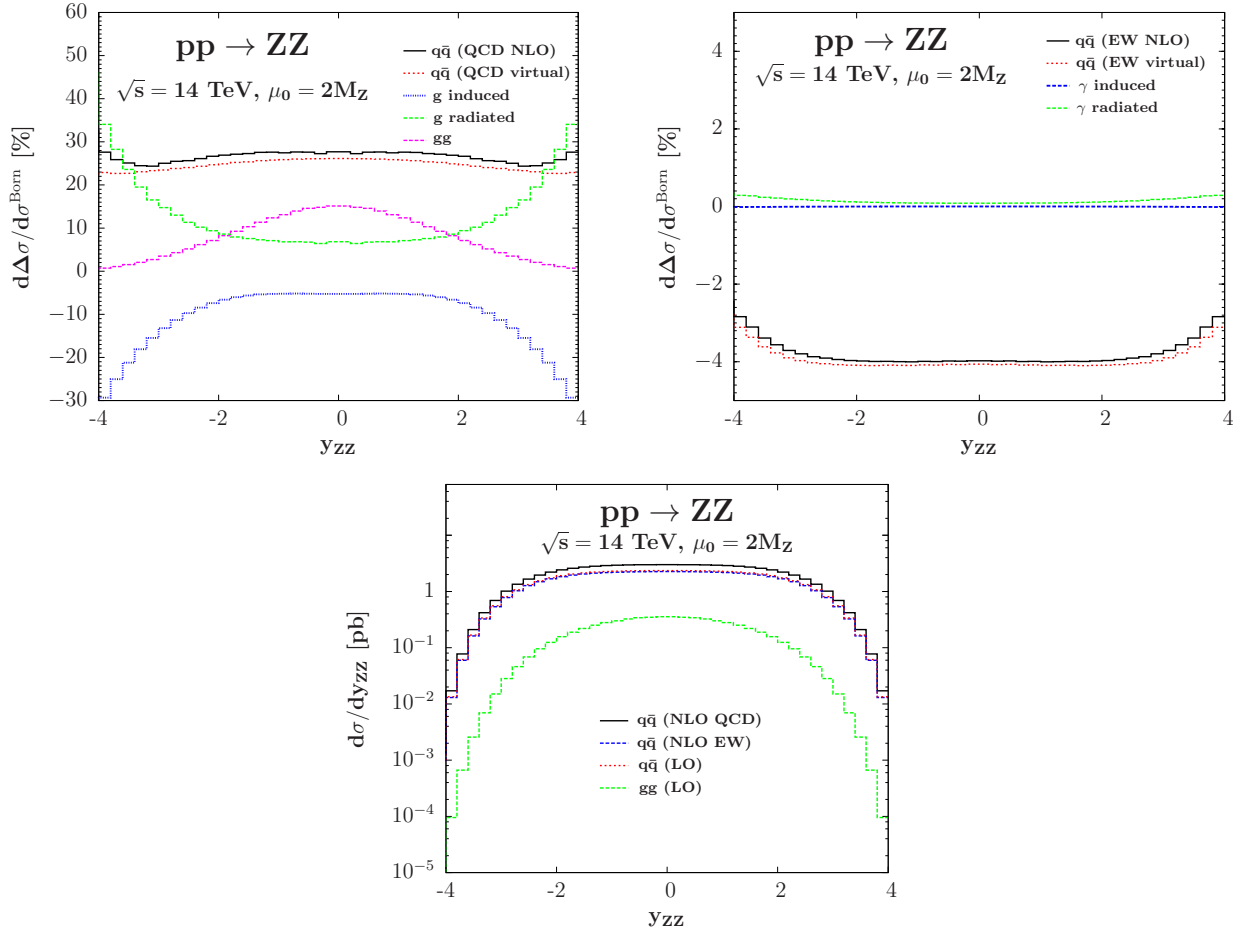


Figure 7: Z pair rapidity y_{ZZ} distribution of the NLO QCD corrections and NLO EW corrections (upper left and right, respectively, in %), as well as the distribution of the $pp \rightarrow ZZ$ cross section (lower, in pb) at the LHC, calculated with MRST2004QED PDF set and with the input parameters described in Section 3.1. The $q\bar{q}$ LO (dotted red) and $q\bar{q}$ NLO EW (dashed blue) curves nearly coincide in the lower panel.

neglected. We also have used the following relations for amplitudes at high energies

$$\begin{aligned}
\mathcal{A}_L^{ug \rightarrow W^+ d} &= \frac{a_W}{c_{L,u}} \mathcal{A}_L^{ug \rightarrow Zu}, \\
\mathcal{A}_L^{dg \rightarrow W^- u} &= \frac{a_W}{c_{L,d}} \mathcal{A}_L^{dg \rightarrow Zd}, \\
\mathcal{A}_L^{dg \rightarrow Zd} &= \frac{c_{L,d}}{c_{L,u}} \mathcal{A}_L^{ug \rightarrow Zu}.
\end{aligned} \tag{14}$$

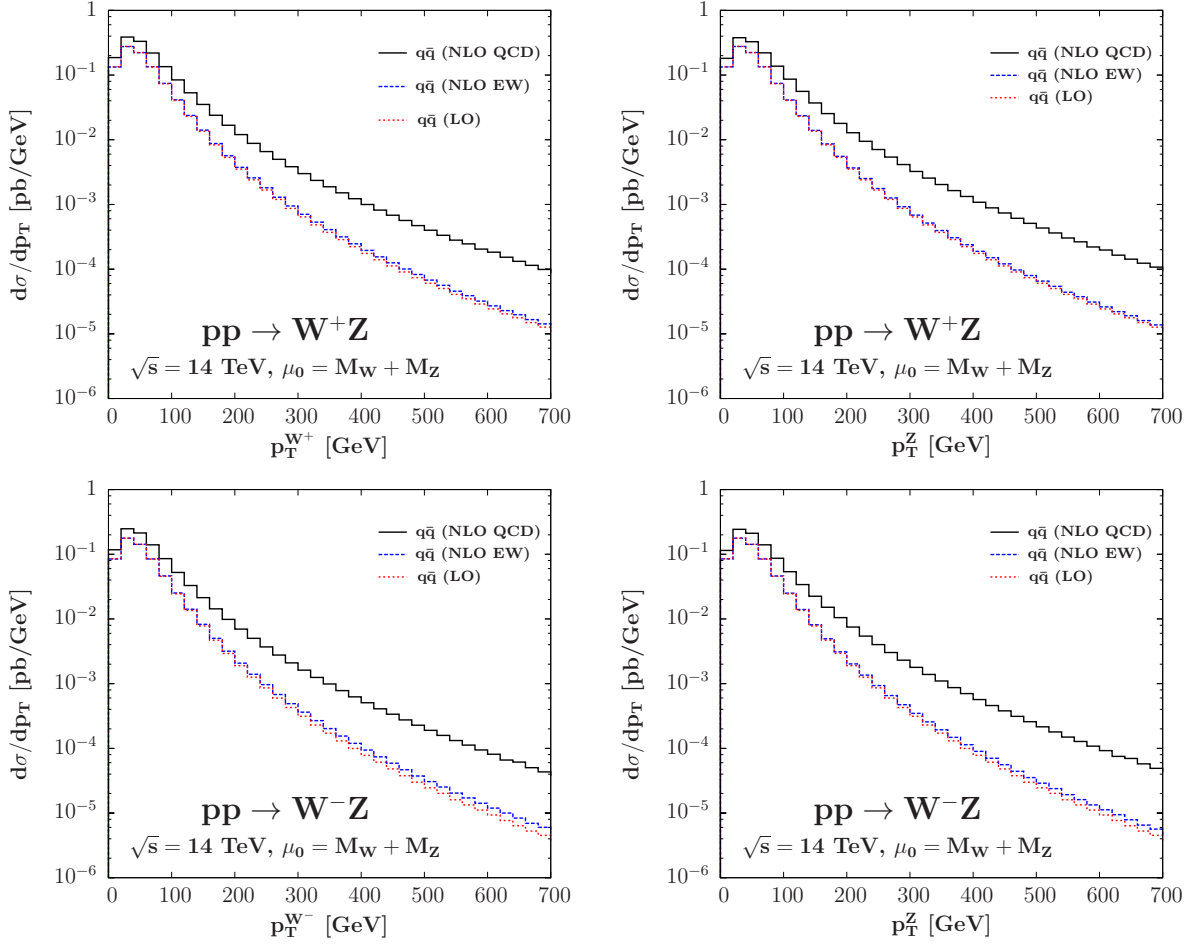


Figure 8: W and Z transverse momentum p_T (in GeV) distributions of $pp \rightarrow W^+Z$ (upper left and right respectively) and $pp \rightarrow W^-Z$ (lower left and right respectively) cross sections at the LHC (in pb/GeV), including NLO QCD and EW corrections calculated with MRST2004QED PDF set and with the input parameters described in Section 3.1. The $q\bar{q}$ LO (dotted red) and $q\bar{q}$ NLO EW (dashed blue) curves nearly coincide.

Doing the same exercise for the $p_T^{W^-}$ distribution we get

$$\begin{aligned}
d\sigma^{dg \rightarrow W^- Z u} &= \frac{1}{2} c_{L,d} c_{L,u} \left(1 + \frac{\cot \theta_W}{c_{L,d}} - \frac{\cot \theta_W}{c_{L,u}} \right) d\sigma_L^{dg \rightarrow W^- u} \frac{\alpha}{2\pi} \log^2 \left[\frac{(p_T^{W^-})^2}{M_Z^2} \right] \\
&= c_{WZ}^d d\sigma_L^{dg \rightarrow Z d} \frac{\alpha}{2\pi} \log^2 \left[\frac{(p_T^{W^-})^2}{M_Z^2} \right], \\
c_{WZ}^d &= \frac{1}{2} a_W^2 \frac{c_{L,u}}{c_{L,d}} \left(1 + \frac{\cot \theta_W}{c_{L,d}} - \frac{\cot \theta_W}{c_{L,u}} \right) = 2.81.
\end{aligned} \tag{15}$$

The huge correction for the p_T^Z distributions can be explained using the same arguments, but we have to consider soft W^\pm radiation instead of soft Z radiation. One has to be careful with the coupling constants because radiating a W^\pm changes the quark flavor. For $p_T^Z \gg M_W$ we

get

$$\begin{aligned}
d\sigma^{ug \rightarrow W^+ Z d} &= c_{WZ}^u d\sigma_L^{ug \rightarrow Zu} \frac{\alpha}{2\pi} \log^2 \left[\frac{(p_T^Z)^2}{M_W^2} \right], \\
d\sigma^{dg \rightarrow W^- Z u} &= c_{WZ}^d d\sigma_L^{dg \rightarrow Zd} \frac{\alpha}{2\pi} \log^2 \left[\frac{(p_T^Z)^2}{M_W^2} \right],
\end{aligned} \tag{16}$$

for W^+Z and W^-Z production, respectively. This result can be obtained from Eqs. (13,15) by replacing M_Z with M_W . This explains why the corrections for the p_T^Z distributions are a little bit larger than the corresponding $p_T^{W^\pm}$ ones. We observe that Eq. (16) differs from the result of Ref. [14]. Numerically, we get $\Delta K_{qg} = 12.61$ (6) and 17.22 (7.60) for leading-logarithmic approximation (full calculation) for $p_T^{W^+}$ and $p_T^{W^-}$ distributions, respectively, at $p_T = 700$ GeV. For p_T^Z distributions, we get $\Delta K_{qg} = 14.22$ (6.30) and 19.42 (9.00) for leading-logarithmic approximation (full calculation) for W^+Z and W^-Z , respectively.

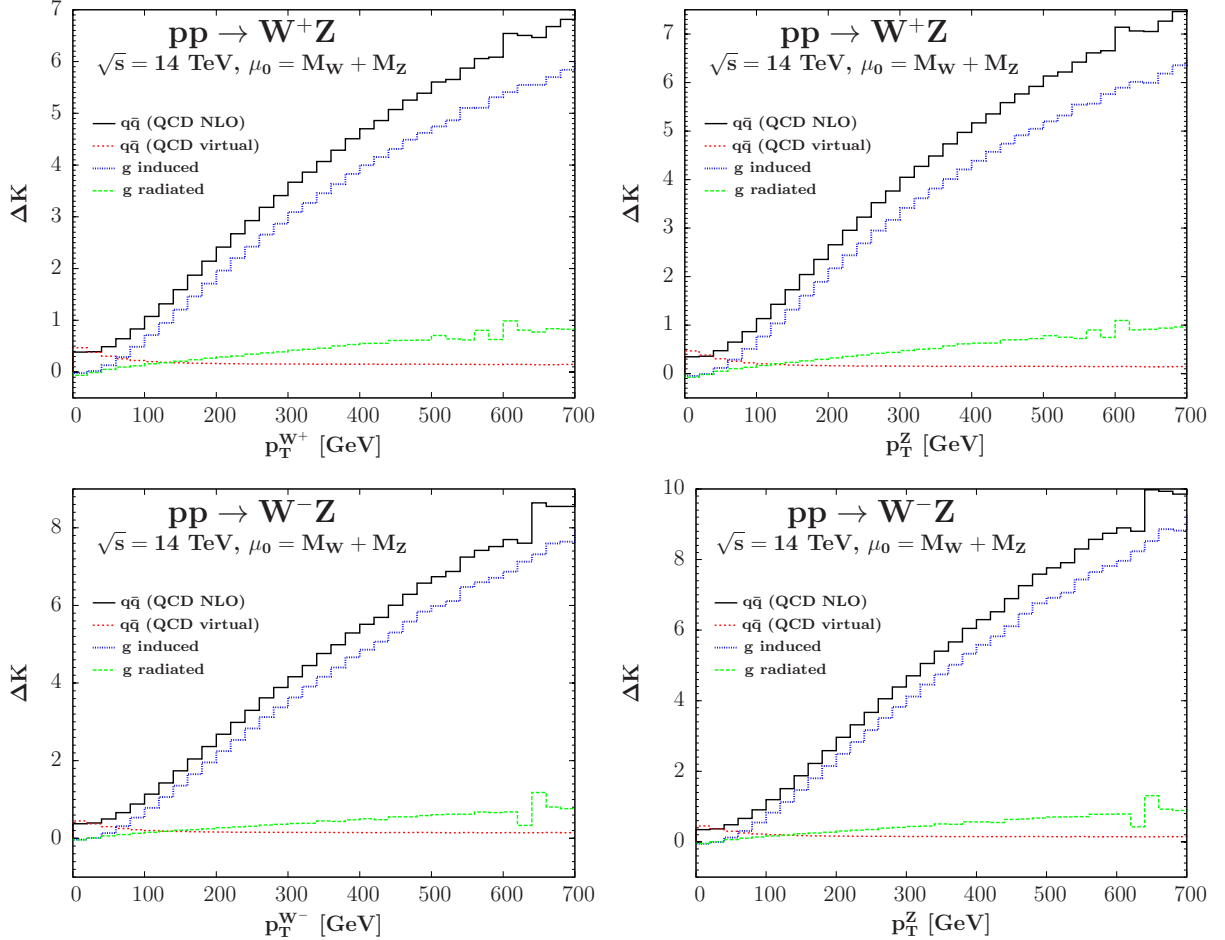


Figure 9: W and Z transverse momentum p_T (in TeV) distributions of the NLO QCD corrections (using ΔK) to $pp \rightarrow W^+Z$ (upper left and right respectively) and $pp \rightarrow W^-Z$ (lower left and right respectively) cross sections at the LHC, calculated with MRST2004QED PDF set and with the input parameters described in Section 3.1.

As for the EW effects, the NLO corrections for the transverse momentum distributions are shown in Fig. 10. In both channels and for both transverse momenta the effect of the

photon radiated processes is negligible. Comparing to the ZZ case, we observe that the virtual correction is significantly less negative. This suggests that there are more cancellations between negative double-logarithm and positive single-logarithm corrections in the $W^\pm Z$ cases. More striking is the difference in the photon-quark induced corrections, it is +60% for the $p_T^{W^-}$ distribution, while only +0.3% for the ZZ case, at 700 GeV. The difference between W^+Z and W^-Z channels is also clearly visible: in the upper panels the photon-quark induced processes (in dotted dashed blue) in the W^+Z channel compensate nearly exactly the effect of the virtual corrections (in dotted red) reducing the total EW corrections to less than $\sim +10\%$ on the whole transverse momentum range both for the W and Z bosons, while in the case of W^-Z process the photon-quark induced corrections are larger, driving the EW corrections to $\sim +30\%$ for $p_T^{W^-} \sim 700$ GeV and $\sim +20\%$ for $p_T^Z \sim 700$ GeV. In both channels the difference with the ZZ channel is much more enhanced than in the QCD case, and the key difference is that the W^\pm can couple to the photon in the EW case. This introduces a new Feynman diagram with t -channel W^\pm exchange in the $2 \rightarrow 2$ process and a new possibility of radiating a soft W^\pm from the initial-state photon. A detailed calculation is presented in the Appendix with all the intermediate steps. To explain the p_T^Z distribution we have to consider soft W^\pm radiation as in the QCD case. For $p_T^Z \gg M_W$ we get

$$\begin{aligned} d\sigma^{u\gamma \rightarrow W^+Zd} &= \left[\frac{1}{2} a_W^2 (1 - a_u + \frac{a_u^2}{2}) d\sigma_L^{u\gamma \rightarrow Zu} + \frac{1}{4} \cot^2 \theta_W d\sigma_L^{u\gamma \rightarrow W^+d} + \frac{1}{4} d\sigma_{LT}^{uW_\gamma^- \rightarrow Zd} \right] \frac{\alpha}{2\pi} \log^2 \left[\frac{(p_T^Z)^2}{M_W^2} \right], \\ d\sigma^{d\gamma \rightarrow W^-Zu} &= \left[\frac{1}{2} a_W^2 (1 - a_d + \frac{a_d^2}{2}) d\sigma_L^{d\gamma \rightarrow Zd} + \frac{1}{4} \cot^2 \theta_W d\sigma_L^{d\gamma \rightarrow W^-u} + \frac{1}{4} d\sigma_{LT}^{dW_\gamma^+ \rightarrow Zu} \right] \frac{\alpha}{2\pi} \log^2 \left[\frac{(p_T^Z)^2}{M_W^2} \right], \end{aligned} \quad (17)$$

where W_γ^\pm means that the photon PDF must be used and

$$a_u = 1 - \frac{Q_d c_{L,d}}{Q_u c_{L,u}}, \quad a_d = 1 - \frac{Q_u c_{L,u}}{Q_d c_{L,d}}. \quad (18)$$

In order to obtain the results in Eq. (17) we have used the following identities, which are true in the high-energy limit,

$$\begin{aligned} \cot \theta_W \mathcal{A}_L^{u\gamma \rightarrow W^+d} - \mathcal{A}_{LT}^{uW^- \rightarrow Zd} &= a_W a_u \mathcal{A}_L^{u\gamma \rightarrow Zu}, \\ \cot \theta_W \mathcal{A}_L^{d\gamma \rightarrow W^-u} - \mathcal{A}_{LT}^{dW^+ \rightarrow Zu} &= -a_W a_d \mathcal{A}_L^{d\gamma \rightarrow Zd}, \end{aligned} \quad (19)$$

where all the gauge bosons are transverse. This is because the longitudinal-mode contributions to Eq. (17) vanish in the high-energy limit $p_T \gg M_Z$. Therefore, all the gauge bosons are transverse in all leading-logarithmic results presented in this paper. More details are given in the Appendix. For $p_T^{W^\pm} \gg M_Z$ with soft Z radiation we have

$$\begin{aligned} d\sigma^{u\gamma \rightarrow W^+Zd} &= \frac{c_{L,u}^2 c_{WZ}^u}{a_W^2} d\sigma_L^{u\gamma \rightarrow W^+d} \frac{\alpha}{2\pi} \log^2 \left[\frac{(p_T^{W^+})^2}{M_Z^2} \right], \\ d\sigma^{d\gamma \rightarrow W^-Zu} &= \frac{c_{L,d}^2 c_{WZ}^d}{a_W^2} d\sigma_L^{d\gamma \rightarrow W^-u} \frac{\alpha}{2\pi} \log^2 \left[\frac{(p_T^{W^-})^2}{M_Z^2} \right]. \end{aligned} \quad (20)$$

The main reason why the photon-quark induced corrections are much larger in the WZ case than in the ZZ case is because the cross sections $d\sigma_L^{d\gamma \rightarrow W^-u}$, $d\sigma_L^{u\gamma \rightarrow W^+d}$, $d\sigma_{LT}^{dW_\gamma^+ \rightarrow Zu}$ and

$d\sigma_{LT}^{uW\gamma^- \rightarrow Zd}$, involving a t -channel Feynman diagram with a gauge boson exchange, are about one to two orders of magnitude larger than $d\sigma_L^{u\gamma \rightarrow Zu}$ at $p_T^Z \approx 700$ GeV. Qualitatively, this can be understood as follows. Considering the ratio of the t -channel Feynman diagram with a gauge boson exchange in $u\gamma \rightarrow W^+d$ to the t -channel Feynman diagram with a quark exchange in $u\gamma \rightarrow Zu$, we get the factor $E_\gamma/|q|$ with $q^2 \approx -2E_\gamma^2(1 - \cos\theta)$ from dimensional analysis. At the amplitude squared level, the factor becomes $1/[2(1 - \cos\theta)]$, which is about 8 for $p_T = 700$ GeV and $E_\gamma = 2$ TeV. Here we are assuming that the dominant contribution comes from the region of 4 TeV of partonic center of mass energy. This is reasonable because, compared to $u\gamma \rightarrow Zu$, the Feynman parameters x_i ($i = 1, 2$) (for dominant contribution) in $u\gamma \rightarrow W^+d$ are expected to be larger due to the exchange of a t -channel gauge boson. Some further enhancement from the couplings can be possible as we have seen in the previous QCD results. Numerically, we get 37.3% (38%), 69.5% (58%) for leading-logarithmic approximation (full calculation) for $p_T^{W^+}$ and $p_T^{W^-}$ distributions, respectively, at $p_T = 700$ GeV. For p_T^Z distributions, we get 58.8% (32%) and 100% (48%) for leading-logarithmic approximation (full calculation) for W^+Z and W^-Z , respectively.

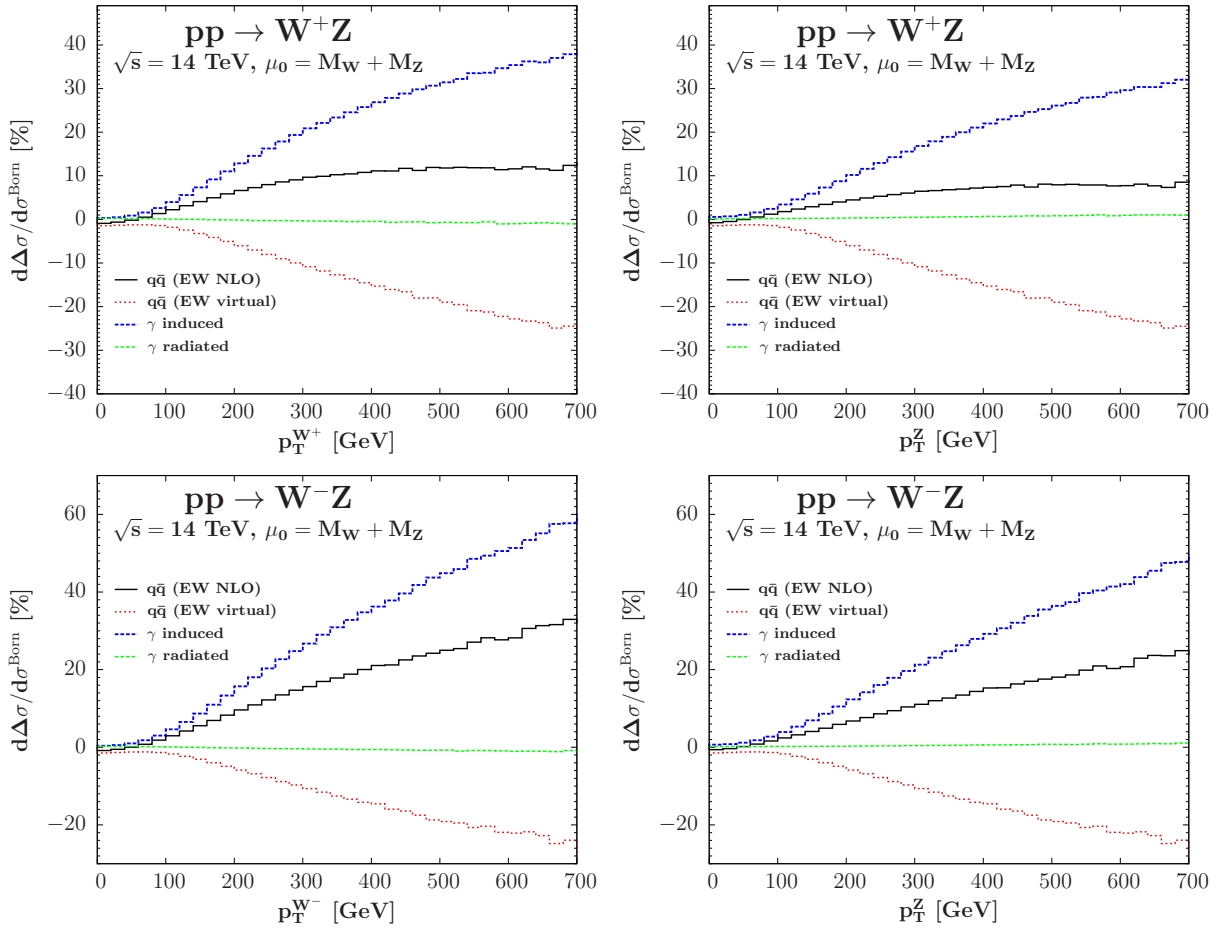


Figure 10: Same as Fig. 9 but for EW corrections (in %).

The invariant mass distributions are similar in W^+Z and W^-Z channels. They are displayed in Fig. 11. The QCD corrections, displayed in middle panels, are of the order of +60% (with some fluctuations up to +70% near the threshold). As displayed in lower panels of Fig. 11 the

EW corrections are very small, $\sim +1\%$ in W^+Z channel for $M_{WZ} \geq 500$ GeV (and close to zero just after the threshold) and $\sim +2\%$ in W^-Z at $M_{WZ} \sim 700$ GeV. We again see a compensation of the virtual Sudakov logarithm (in dotted red), giving a decreasing virtual corrections down to -4% in both channels, to be added to the positive correction coming from the photon-quark induced processes (dotted dashed blue) up to $\sim +4\%$ in W^+Z channel and $\sim +5\%$ in W^-Z channel.

We end the study of W^+Z and W^-Z channels with the rapidity distributions of the WZ pair displayed in Fig. 12. W^+Z and W^-Z channels have a slightly different shape, the former channel having a double gaussian shape with a minimum around $y_{WZ} = 0$ while the latter displays a gaussian shape with a maximum around $y_{WZ} = 0$. The EW corrections are negligible, no more than $\sim +3\%$ ($\sim +2\%$) in W^+Z channel (W^-Z channel), as depicted in the lower panels of Fig. 12, compared to the $\sim +40$ – 60% increase due to the QCD corrections as seen in the middle panels. The photon-quark induced processes play a very important role in the EW corrections: while the virtual corrections are always negative from $\sim -1\%$ down to $\sim -2\%$ at $y_{WZ} = 0$ in both channels, the photon-quark induced processes are always positive with a gaussian shape in both channels, resulting in a mexican hat shape for the EW corrections, sharper in the W^+Z channel than in the W^-Z channel.

3.4 WW distributions

We do the same exercise as above for $pp \rightarrow W^+W^-$ channel. The distributions of the transverse momentum $p_T^{W^+}$ of the W^+ and the WW invariant mass are shown in Fig. 13 and show a similar behavior as for ZZ production. Notable is the contribution of the $\gamma\gamma$ induced process. In the $p_T^{W^+}$ distribution it is only slightly smaller than the gg contribution except at small p_T . Its contribution to the WW invariant mass distribution is about one order of magnitude smaller than the gg induced process at low invariant masses while it is about a factor 2 larger at $M_{WW} \simeq 700$ GeV. The trend that is seen in Fig. 14 for the $p_T^{W^+}$ and M_{WW} distributions of the QCD corrections is the same as the one seen in Fig. 5 for ZZ production. The QCD corrections in the $p_T^{W^+}$ distribution are driven by a double-logarithmic enhancement in the gluon-quark induced subprocesses and one has up to a $\Delta K \sim 3$ correction at $p_T^{W^+} = 700$ GeV.

Similar to the ZZ and WZ cases, to explain the $p_T^{W^+}$ distribution we have to consider soft W^- radiation. For $p_T^{W^+} \gg M_W$, keeping only the leading corrections, we get

$$d\sigma^{qg \rightarrow W^+W^-q} = c_{WW}^q d\sigma_L^{qg \rightarrow Zq} \frac{\alpha}{2\pi} \log^2 \left[\frac{(p_T^{W^+})^2}{M_W^2} \right],$$

$$c_{WW}^q = \frac{a_W^4}{2c_{L,q}^2}, \quad q = u, d. \quad (21)$$

For the sake of comparison with c_{ZZ}^q and c_{WZ}^q , we have $c_{WW}^u = 3.53$ and $c_{WW}^d = 2.40$. Numerically, for the $p_T^{W^+}$ distribution, we get $\Delta K_{qg} = 5.33$ (3.10) for leading-logarithmic approximation (full calculation) at $p_T = 700$ GeV.

In the invariant mass distribution the gluon-quark induced and the gluon-quark radiated processes compensate each other and the full QCD corrections are dominated by the virtual corrections. The gluon fusion mechanism amounts to $\sim +5\%$ in the M_{WW} distribution and is negligible in the transverse momentum distribution.

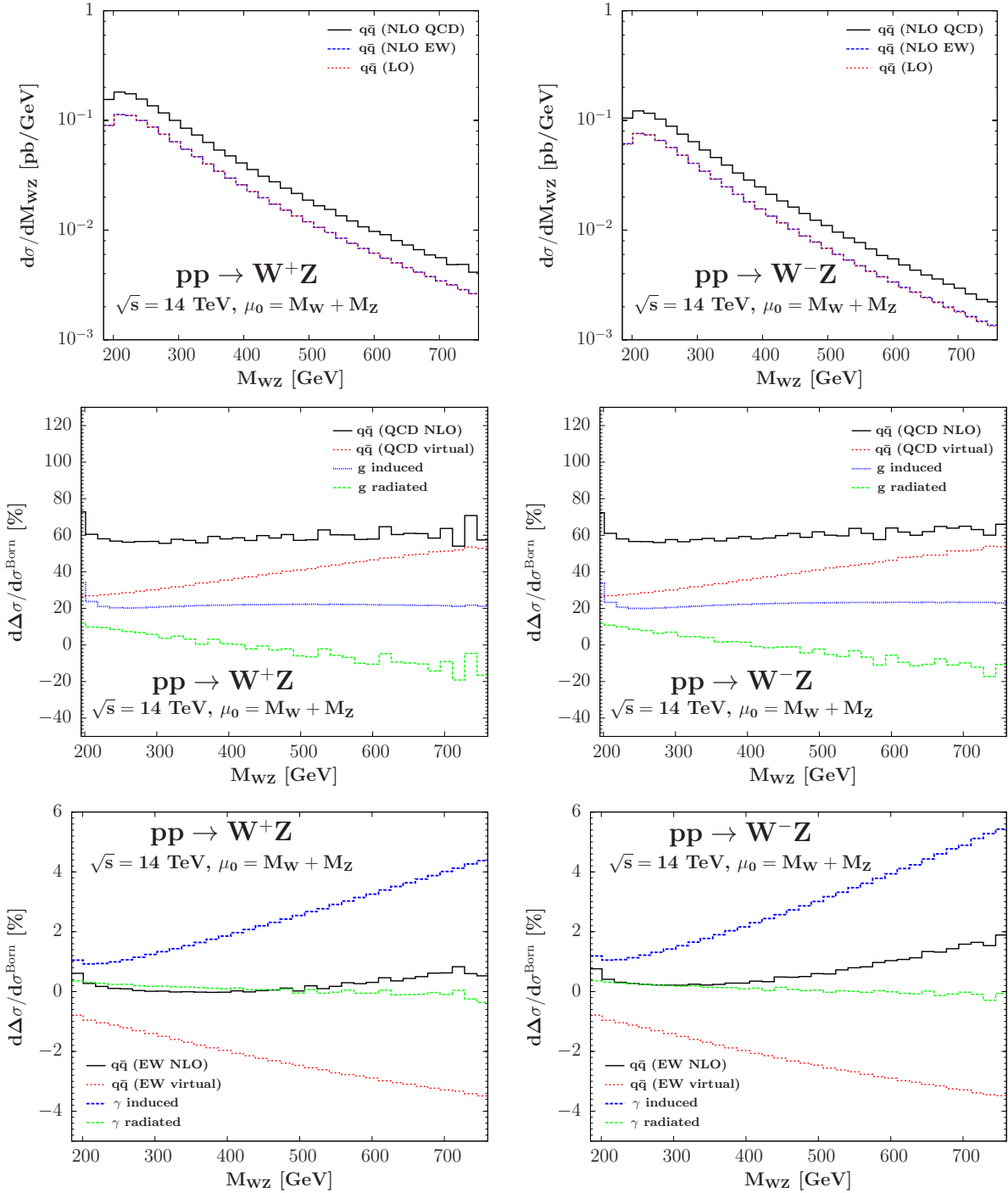


Figure 11: M_{WZ} invariant mass (in GeV) distribution of $pp \rightarrow W^+Z$ (upper left) and $pp \rightarrow W^-Z$ (upper right) cross sections at the LHC (in pb/GeV), including NLO QCD and EW corrections calculated with MRST2004QED PDF set and with the input parameters described in Section 3.1. The $q\bar{q}$ LO (dotted red) and $q\bar{q}$ NLO EW (dashed blue) curves nearly coincide. Middle left (right) panels: M_{WZ} invariant mass distribution of the NLO QCD corrections to $pp \rightarrow W^+Z$ ($pp \rightarrow W^-Z$) cross section at the LHC (in %); lower left and right: the same but for the NLO EW corrections.

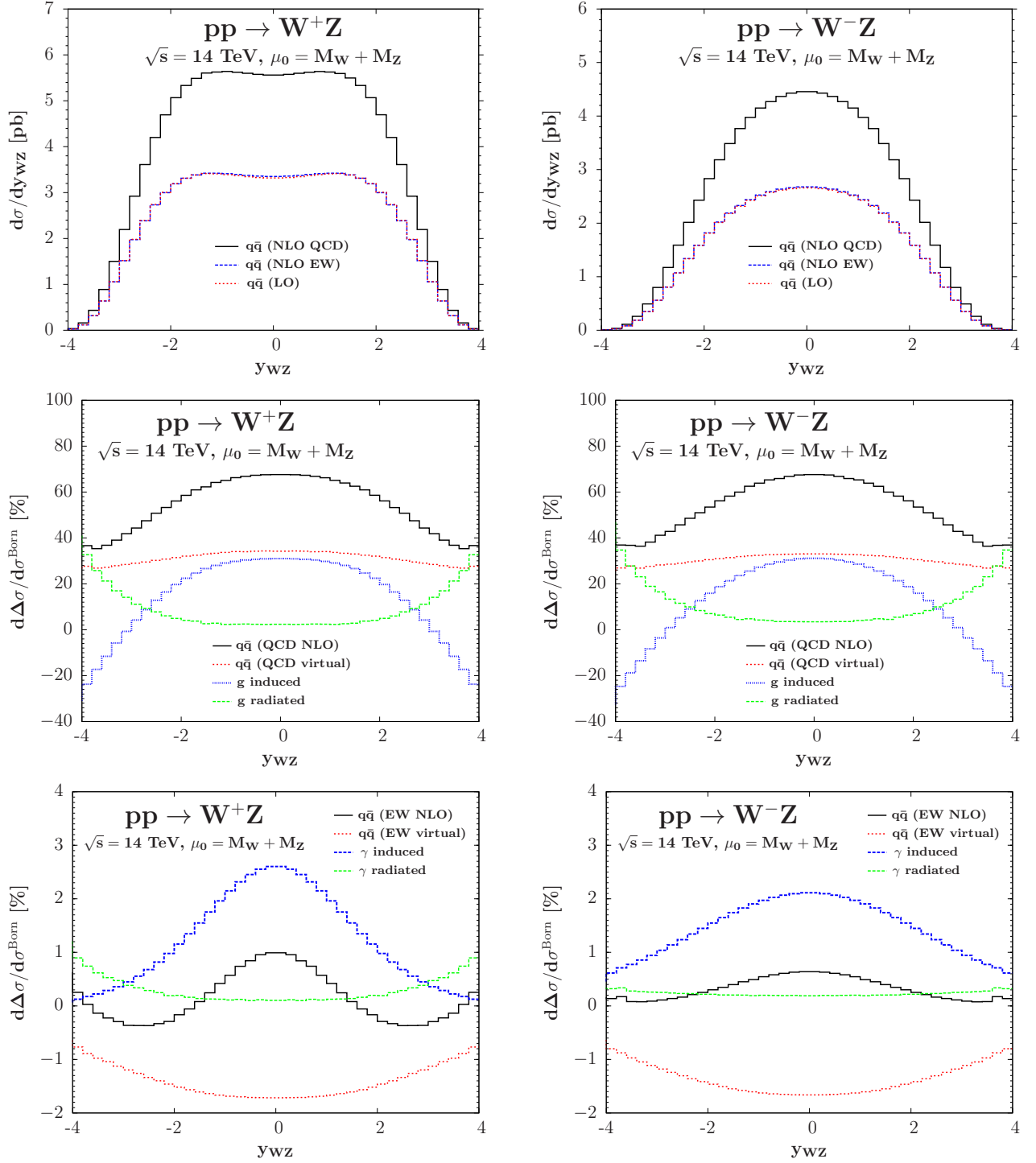


Figure 12: WZ pair rapidity y_{WZ} distributions of $pp \rightarrow W^+Z$ (upper left, in pb) and $pp \rightarrow W^-Z$ (upper right, in pb) as well as the y_{WZ} distributions of the NLO QCD corrections and the NLO EW corrections in $pp \rightarrow W^+Z$ channel (middle left and lower left, respectively, in %) and in $pp \rightarrow W^-Z$ channel (middle right and lower right, respectively), at the LHC, calculated with MRST2004QED PDF set and with the input parameters described in Section 3.1. The $q\bar{q}$ LO (dotted red) and $q\bar{q}$ NLO EW (dashed blue) curves nearly coincide in the upper panels.

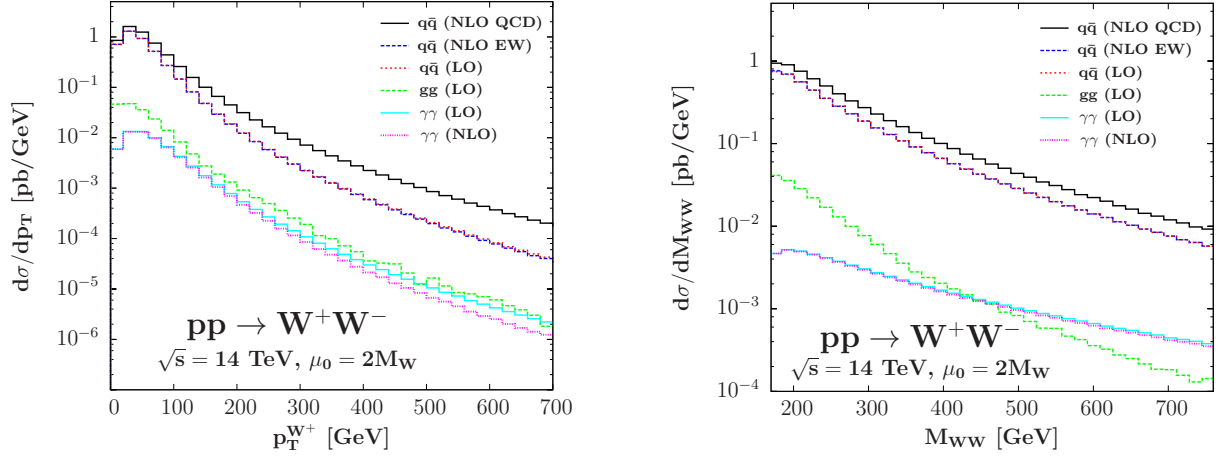


Figure 13: W^+ transverse momentum p_T (in GeV) distribution (left) and W pair invariant mass M_{WW} (in GeV) distribution (right) of $pp \rightarrow WW$ cross section at the LHC (in pb/GeV), including NLO QCD and EW corrections calculated with MRST2004QED PDF set and with the input parameters described in Section 3.1. The LO $q\bar{q}$ (dotted red) and NLO EW $q\bar{q}$ (dashed blue) curves nearly coincide, as well as the LO $\gamma\gamma$ (solid light blue) and NLO $\gamma\gamma$ (dotted violet) in the M_{WW} distribution.

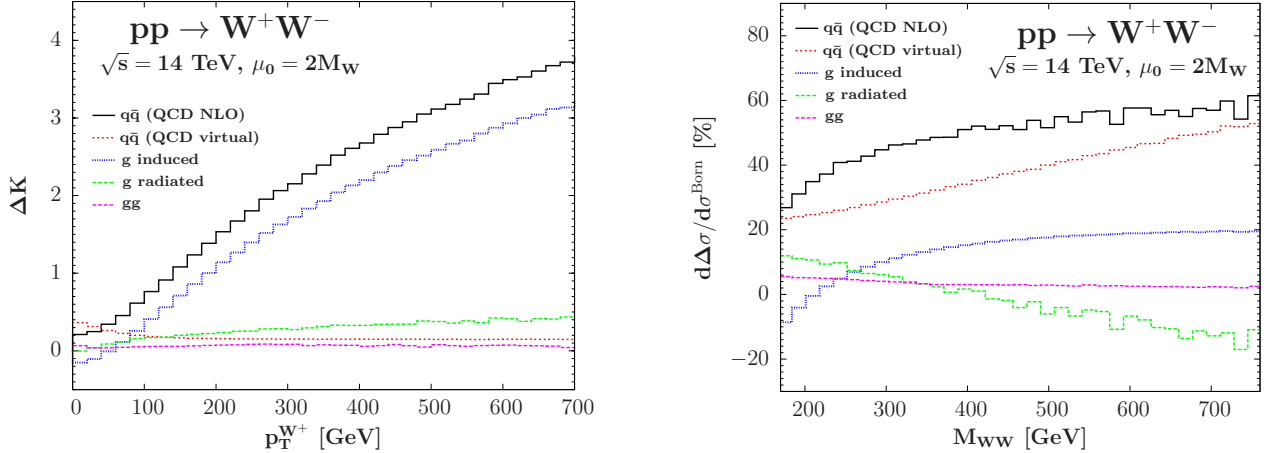


Figure 14: W^+ transverse momentum p_T (in TeV) distribution (left, using ΔK) and W pair invariant mass M_{WW} (in GeV) distribution (right, in %) of the NLO QCD corrections to $pp \rightarrow WW$ cross section at the LHC, calculated with MRST2004QED PDF set and with the input parameters described in Section 3.1.

Turning to EW corrections, we observe that the effect of the virtual Sudakov logarithms $\alpha \log^2[(p_T^{W^+})^2/M_W^2]$ is clearly visible in Fig. 15 (left) where the dotted red curve is the $p_T^{W^+}$ distribution of the virtual EW corrections, and we have a -30% correction at $p_T^{W^+} = 600$ GeV. The interesting point is again that this Sudakov logarithm is compensated by the effect of photon-quark induced processes displayed in dotted-dashed blue as already seen in the case of WZ distributions. Eventually the EW corrections in the $q\bar{q}$ subprocesses are limited and not more than -10% over the whole p_T range. The same effect is visible in the invariant mass distribution, where the total EW corrections to the $q\bar{q}$ subprocesses drop very fast from $+2\%$ at the threshold to small variations around zero. As in the case of WZ , by considering the

limit of soft W^- radiation we get for $p_T^{W^+} \gg M_W$

$$\begin{aligned} d\sigma^{u\gamma \rightarrow W^+W^-u} &= \left(\frac{a_W^4}{4c_{L,u}^2} d\sigma_L^{u\gamma \rightarrow Zu} + \frac{a_W^2}{4} d\sigma_L^{u\gamma \rightarrow W^+d} + \frac{1}{4} d\sigma_{LT}^{uW_\gamma^+ \rightarrow W^+u} \right) \frac{\alpha}{2\pi} \log^2 \left[\frac{(p_T^{W^+})^2}{M_W^2} \right], \\ d\sigma^{d\gamma \rightarrow W^+W^-d} &= \left(\frac{a_W^4}{4c_{L,d}^2} d\sigma_L^{d\gamma \rightarrow Zd} + \frac{a_W^2}{4} d\sigma_L^{u_d\gamma \rightarrow W^+d} + \frac{1}{4} d\sigma_{LT}^{dW_\gamma^+ \rightarrow W^+d} \right) \frac{\alpha}{2\pi} \log^2 \left[\frac{(p_T^{W^+})^2}{M_W^2} \right], \end{aligned} \quad (22)$$

where u_d means that the d PDF must be used. And for the limit of soft W^+ radiation with $p_T^{W^-} \gg M_W$ we have

$$\begin{aligned} d\sigma^{u\gamma \rightarrow W^+W^-u} &= \left(\frac{a_W^4}{4c_{L,u}^2} d\sigma_L^{u\gamma \rightarrow Zu} + \frac{a_W^2}{4} d\sigma_L^{d_u\gamma \rightarrow W^-u} + \frac{1}{4} d\sigma_{LT}^{uW_\gamma^- \rightarrow W^-u} \right) \frac{\alpha}{2\pi} \log^2 \left[\frac{(p_T^{W^-})^2}{M_W^2} \right], \\ d\sigma^{d\gamma \rightarrow W^+W^-d} &= \left(\frac{a_W^4}{4c_{L,d}^2} d\sigma_L^{d\gamma \rightarrow Zd} + \frac{a_W^2}{4} d\sigma_L^{d\gamma \rightarrow W^-u} + \frac{1}{4} d\sigma_{LT}^{dW_\gamma^- \rightarrow W^-d} \right) \frac{\alpha}{2\pi} \log^2 \left[\frac{(p_T^{W^-})^2}{M_W^2} \right], \end{aligned} \quad (23)$$

where d_u means that the u PDF must be used. Similar to the WZ case, only the transverse gauge bosons contribute and we have used the following identities in the high-energy limit,

$$\begin{aligned} a_W \mathcal{A}_L^{u\gamma \rightarrow W^+d} - \mathcal{A}_{LT}^{uW^+ \rightarrow W^+u} &= \frac{a_W^2}{c_{L,u}} \mathcal{A}_L^{u\gamma \rightarrow Zu}, \\ a_W \mathcal{A}_L^{d\gamma \rightarrow W^-u} - \mathcal{A}_{LT}^{uW^- \rightarrow W^-u} &= \frac{a_W^2}{c_{L,u}} \mathcal{A}_L^{u\gamma \rightarrow Zu}, \\ a_W \mathcal{A}_L^{d\gamma \rightarrow W^-u} + \mathcal{A}_{LT}^{dW^- \rightarrow W^-d} &= \frac{a_W^2}{c_{L,d}} \mathcal{A}_L^{d\gamma \rightarrow Zd}, \\ a_W \mathcal{A}_L^{u\gamma \rightarrow W^+d} + \mathcal{A}_{LT}^{dW^+ \rightarrow W^+d} &= \frac{a_W^2}{c_{L,d}} \mathcal{A}_L^{d\gamma \rightarrow Zd}. \end{aligned} \quad (24)$$

Numerically, for the $p_T^{W^+}$ distribution, we get 22% (26%) for leading-logarithmic approximation (full calculation) at $p_T = 700$ GeV. As in the WZ case, the large photon-quark induced corrections are due to the hard $2 \rightarrow 2$ amplitudes with a t -channel gauge boson exchange.

The $\gamma\gamma$ subprocess has more impact on the invariant mass distribution than on the transverse momentum one, increasing up to +6% at about 700 GeV. As expected, the NLO corrections in the $\gamma\gamma$ subprocess are dominated by the negative Sudakov-logarithm corrections from the virtual part, as can be seen in the $p_T^{W^+}$ distribution.

We also display the rapidity distribution of the W pair in Fig. 16. As can be seen on the lower panel of Fig. 16 the impact of NLO corrections on the diphoton sub-channel is negligible in the rapidity distribution. The impact of the diphoton and gluon fusion channels are two to three order of magnitudes less than the NLO QCD corrections to the $q\bar{q}$ sub-channels, as already seen in previous analyses, while the total EW corrections (including diphoton corrections) are limited as they amount to less than $\sim +2\%$ and are always positive. The upper right panel of Fig. 16 gives another example of the important impact of the photon-quark induced processes in the structure of the EW corrections on W pair production: while the EW virtual corrections display a negative quadratic behavior with a minimum at $y_{WW} \sim 0$, the photon-quark induced processes

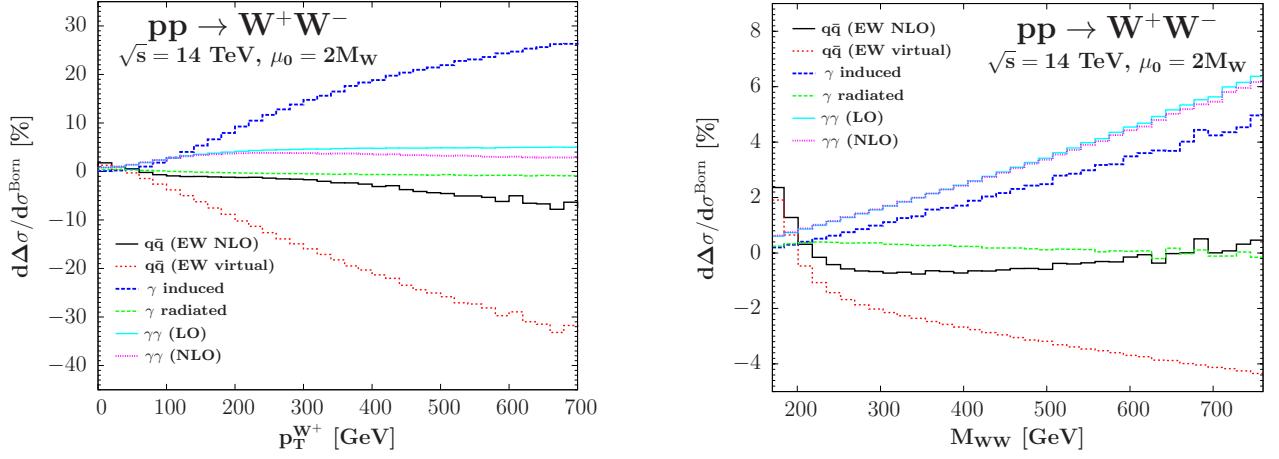


Figure 15: Same as Fig. 14 but for EW corrections (in %). The LO $\gamma\gamma$ (solid light blue) and NLO $\gamma\gamma$ (dotted violet) curves coincide in the M_{WW} distribution.

give a positive contribution which in addition modifies the shape of the EW corrections into a mexican hat shape with two degenerate positive minima at $|y_{WW}| \sim 2$. The photon radiated processes give a small contribution of less than +0.5% on the whole rapidity range considered and the diphoton corrections are dominant for $|y_{WW}| \leq 3\%$.

From the above discussion about the huge QCD corrections originating from the gluon-quark induced processes, we may think of using a jet veto (i.e. veto events with $p_{T,\text{jet}} > p_{\text{veto}}$) to reduce those corrections. This issue has been studied in Ref. [63] for a similar process of WWZ production at the LHC. There it is found that using a dynamic jet veto such as $p_{\text{veto}} = \text{Max}(M_{T,V}, M_{T,V'})/2$ with $M_{T,V} = (p_{T,V}^2 + M_V^2)^{1/2}$ being the transverse mass reduces significantly the QCD corrections and gives a stable result. Using a fixed jet veto such as $p_{\text{veto}} = 25$ GeV is not a good idea because it over-subtracts the QCD corrections and creates large negative corrections at large $p_{T,V}$. However, the price to pay is that the theoretical uncertainty gets larger for exclusive observables with jet veto, see e.g. Refs. [63, 64].

3.5 Discussion of the leading-logarithmic approximation

We have seen in the previous subsections that the leading-logarithmic approximation gives a good explanation why the QCD (EW) corrections arising from the gluon (photon)-quark induced processes are largest for the WZ case and smallest for the ZZ case. In order to have more insights into this hierarchy, we compare the QCD results at the same value of $p_T \gg M_Z$ so that the double-logarithmic factors are approximately equal and can be ignored. We have

$$\begin{aligned}
\frac{d\sigma^{qg \rightarrow ZZq}}{d\sigma^{\bar{q}q \rightarrow ZZ}} &\propto 2c_{ZZ}^u \frac{d\sigma_L^{ug \rightarrow Zu}}{d\sigma^{\bar{q}q \rightarrow ZZ}}, \\
\frac{d\sigma^{ug \rightarrow W^+Zd}}{d\sigma^{u\bar{d} \rightarrow W^+Z}} &\propto c_{WZ}^u \frac{d\sigma_L^{ug \rightarrow Zu}}{d\sigma^{u\bar{d} \rightarrow W^+Z}}, \\
\frac{d\sigma^{qg \rightarrow W^+W^-q}}{d\sigma^{\bar{q}q \rightarrow W^+W^-}} &\propto c_{WW}^u \frac{d\sigma_L^{ug \rightarrow Zu}}{d\sigma^{\bar{q}q \rightarrow W^+W^-}},
\end{aligned} \tag{25}$$

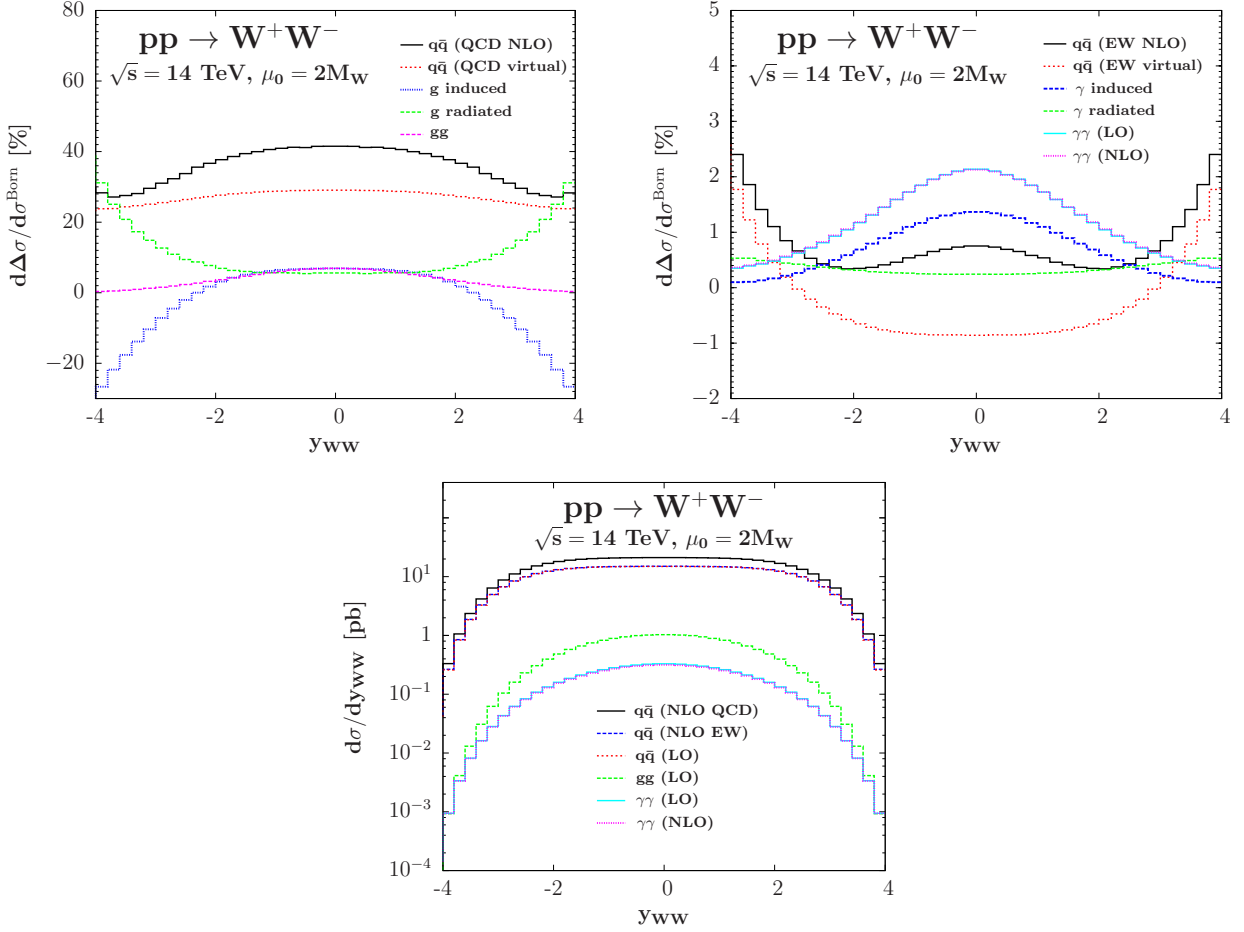


Figure 16: W pair rapidity y_{WW} distribution of the NLO QCD corrections and NLO EW corrections (upper left and right, respectively, in %), as well as the distribution of the $pp \rightarrow WW$ cross section (lower, in pb) at the LHC, calculated with MRST2004QED PDF set and with the input parameters described in Section 3.1. The LO $\gamma\gamma$ (solid light blue) and NLO $\gamma\gamma$ (dotted violet) curves coincide as well as the LO $q\bar{q}$ (dotted red) and NLO EW $q\bar{q}$ (dashed blue) in the lower panel.

where we have used the fact that $c_{ZZ}^d d\sigma_L^{dg \rightarrow Zd} \approx c_{ZZ}^u d\sigma_L^{ug \rightarrow Zu}$ which is a consequence of the two properties: the Z boson couples more strongly to the d quarks than to the u quarks, but the d PDF is smaller than the u PDF. Thus, the hierarchy of the numerators is $c_{WZ}^u : c_{WW}^u : 2c_{ZZ}^u = 4.13 : 3.53 : 0.36$. We observe a clear difference between the WV ($V = Z, W$) channels and the ZZ channel due to the fact that the former includes trilinear gauge couplings, and also because of the fact that the quarks couple more strongly to the W than to the Z bosons. The hierarchy of the denominators is $d\sigma^{\bar{q}q \rightarrow W^+W^-} : d\sigma^{u\bar{d} \rightarrow W^+Z} : d\sigma^{\bar{q}q \rightarrow ZZ} = 4.54 : 1.35 : 1$. This hierarchy due to different PDFs and different coupling strengths is more reduced compared to the one of the numerators. To sum up, the hierarchy observed in the QCD gluon-quark induced corrections comes from trilinear gauge couplings, different coupling strengths, and different PDFs. For the EW photon-quark induced corrections, a larger hierarchy occurs. This is because, in addition to the above mechanisms, there is a new dynamical enhancement in the numerators for the WV channels, namely the contributions $d\sigma_L^{u\gamma \rightarrow W^+d}$ and $d\sigma_{LT}^{uW^+ \rightarrow W^+u}$ with a t -channel exchange of a gauge boson are from one to two orders of magnitude higher than $d\sigma_L^{u\gamma \rightarrow Zu}$.

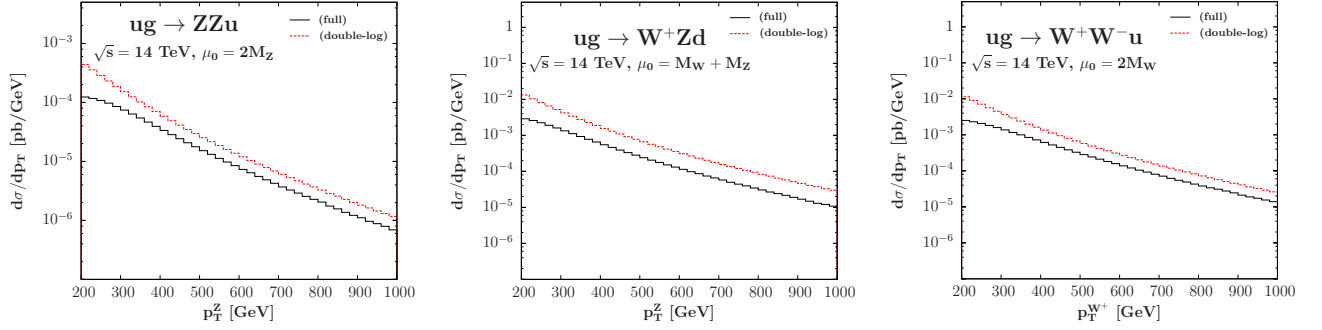


Figure 17: Comparison between the full results (plain black line) and the analytical leading-logarithmic approximation (dashed red line) for gluon-quark induced processes in ZZ (left), W^+Z (middle) and WW (right) p_T differential distributions.

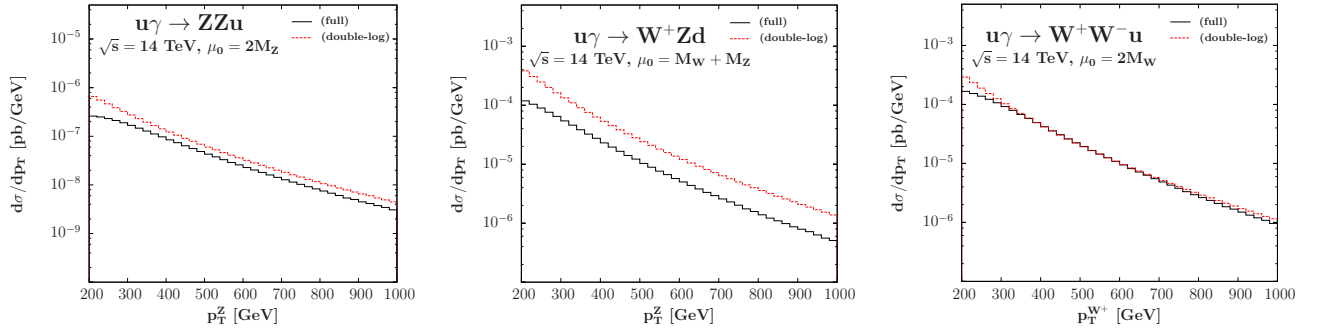


Figure 18: Same as Fig. 17 but for photon-quark induced processes.

We observe, however, that the leading-logarithmic approximation can differ from the full result by up to a factor of two in the case of WZ production. This could trigger concerns about our explanation of the hierarchy between the different diboson production channels. In order to validate our calculation we display in this subsection the comparison between the full result and the analytical approximation at high transverse momentum. In Fig. 17 are displayed the results for the gluon-quark induced processes. We only show the full results without the subtraction term and we have used a transverse momentum cut $p_T^q > 200$ GeV both in the full result and in the analytical approximation. We have checked that the IR subtraction terms included in the gluon-quark induced and photon-quark induced contributions in the previous subsections are very small at large transverse momentum ($p_T > 500$ GeV). In all cases the analytical approximation is larger than the full results. The difference shows the impact of single-logarithm terms that are particularly sizable in the WZ channel. To have a numerical feeling for the difference between double and single logarithmic corrections, assuming that the correction pre-factors are the same, we get, as a ratio between double and single logarithmic contributions, $\log(p_T^2/M_W^2)$ about 5 at $p_T = 1$ TeV and 20 at 10^3 TeV. We have checked that the double-logarithmic contributions almost coincide with the full results at $p_T = 10^3$ TeV at a hypothetical super hadron collider.

The same comparison has been done in the case of photon-quark induced processes. This is displayed in Fig. 18 below. In all channels the agreement is better in the case of EW corrections compared to QCD corrections, in particular in the WW channel where the agreement is almost perfect already at $p_T \simeq 700$ GeV.

3.6 Contributions from third-generation external quarks

In this section we discuss the contributions with a b quark in the initial state. This is of relevance only for the WW and ZZ cases because final states with a t quark occurring in the WZ case lead to different experimental signatures and are therefore excluded. This contribution is suppressed in the ZZ case and at LO in the W^+W^- case due to small b PDF. For the W^+W^- final state, there is a new enhancement mechanism in the hard amplitude with an intermediate on-shell top quark, as noticed in Ref. [27]. This occurs at NLO as shown in Fig. 19 for the gluon-quark

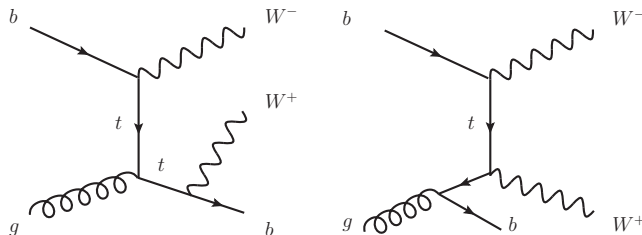


Figure 19: Representative t -channel diagrams for $bg \rightarrow W^+W^-b$ production cross section.

induced process $bg \rightarrow W^+W^-b$. Only representative t -channel diagrams are displayed but the discussion is similar for the s -channel diagrams. The left-hand side of Fig. 19 is a typical single top production channel diagram, $bg \rightarrow tW^-$ followed by the decay $t \rightarrow W^+b$ with branching ratio close to one. The right-hand side diagram is essentially $b\bar{b} \rightarrow W^+W^-$ with one initial b quark originated from the gluon splitting. The large tW production mode, being a part of the single-top background, should be excluded and our main concern is the interference between the two mechanisms. We have estimated this effect and found that, for $\sqrt{s} = 14$ TeV, the correction is at the per mille level compared to the full NLO total cross section. We therefore conclude that, after the subtraction of the single-top contribution, the contribution from processes with initial b quarks can be neglected.

4 Total cross sections and theoretical uncertainties

In order to make a comparison with experimental results, a thorough assessment of theoretical uncertainties affecting the central predictions of the total cross sections is needed. In this section we will consider three sources of uncertainties: the scale uncertainty which is an estimate of the missing higher-order terms in the perturbative calculation, the uncertainty related to the parton distribution functions and the fitted value of the strong coupling constant $\alpha_s(M_Z^2)$ and the parametric uncertainties related to the experimental errors on W and Z masses, $M_W = (80.385 \pm 0.015)$ GeV and $M_Z = (91.1876 \pm 0.0021)$ GeV.

As for the last source of uncertainties mentioned above, we have checked that it actually does not affect our predictions more than $\pm 0.2\%$ at all c.m. energies in all diboson channels. We will then ignore the parametric errors in the final combination of the theoretical uncertainties.

In order to include the full NLO QCD+EW effects using different PDF sets, the calculation is done in two steps. First, using MRST2004QED PDF set [45] which includes the photon PDF

as described in Section 2, we calculate the EW correction factor as

$$\delta_{\text{EW}} = \frac{\sigma^{\text{QCD+EW, MRSTQED}}}{\sigma^{\text{QCD, MRSTQED}}}, \quad (26)$$

where the numerator is the full result including also the gluon fusion and the $\gamma\gamma$ channel at NLO (for the WW case), while the denominator is without the NLO EW corrections and the $\gamma\gamma$ contribution. We then calculate the full NLO QCD correction using another PDF set, e.g. MSTW2008 set [62], and rescale it with the above EW correction factor to get

$$\sigma_{\text{MSTW}}^{\text{QCD+EW}} = \delta_{\text{EW}} \times \sigma_{\text{MSTW}}^{\text{QCD}}. \quad (27)$$

We use the same parameter setup as in Section 3, save the value of $\alpha_s(M_Z^2)$ that is adapted according to the PDF set used. In the case of MSTW2008 PDF set that we will use as our default set, we will use $\alpha_s^{\text{NLO}}(M_Z^2) = 0.12018$ and $\alpha_s^{\text{NNLO}}(M_Z^2) = 0.11707$ as central values. The NNLO value (and running) of the strong coupling constant is used for $gg \rightarrow WW, ZZ$ subprocesses as well as the NNLO gluon PDF when available. Otherwise the strong coupling constant gets its NLO value and the running is also evaluated at NLO.

We have found that EW corrections are negligible in the WZ channels. In the case of WW channel we have found $\delta_{\text{EW}}^{WW} \sim +1.5\%$ mainly due to the $\gamma\gamma$ contribution while in the case of ZZ channel the correction is negative and sizable, $\delta_{\text{EW}}^{ZZ} \sim -3\%$ due to the EW virtual corrections, with nearly no energy dependence for both production channels. Note that this EW factor is the size of the EW corrections on top of the full NLO QCD predictions.

4.1 Scale uncertainty

As the calculation is done in the perturbative framework, the theoretical cross sections depend on two unphysical scales: the renormalization scale μ_R that comes from the running of α_s , and the factorization scale μ_F that comes from the convolution of the perturbative partonic cross section with the non-perturbative parton distribution functions. The variation of the cross sections with respect to these two scales can be viewed as an estimate of the missing higher-order corrections and this is the first uncertainty that is considered in this paper. We choose the interval

$$\frac{1}{2}\mu_0 \leq \mu_R = \mu_F \leq 2\mu_0, \quad (28)$$

where μ_0 is the central scale for the process under study and has been defined in the previous section.

As can be seen in Fig. 20, the scale uncertainty is limited in the different gauge boson pair production channels: we obtain $\sim +3\%/ - 2.5\%$ at 7 TeV in WW and ZZ channels, slightly more in WZ channels with $\sim +5\%/ - 4\%$ at 7 TeV. It then reduces down to less than 1% at 33 TeV in all diboson production channels.

4.2 PDF+ α_s uncertainty

The other main source of theoretical uncertainty is the parametrization of the parton distribution functions (PDF). Indeed the calculation of an hadronic cross section is done in two parts:

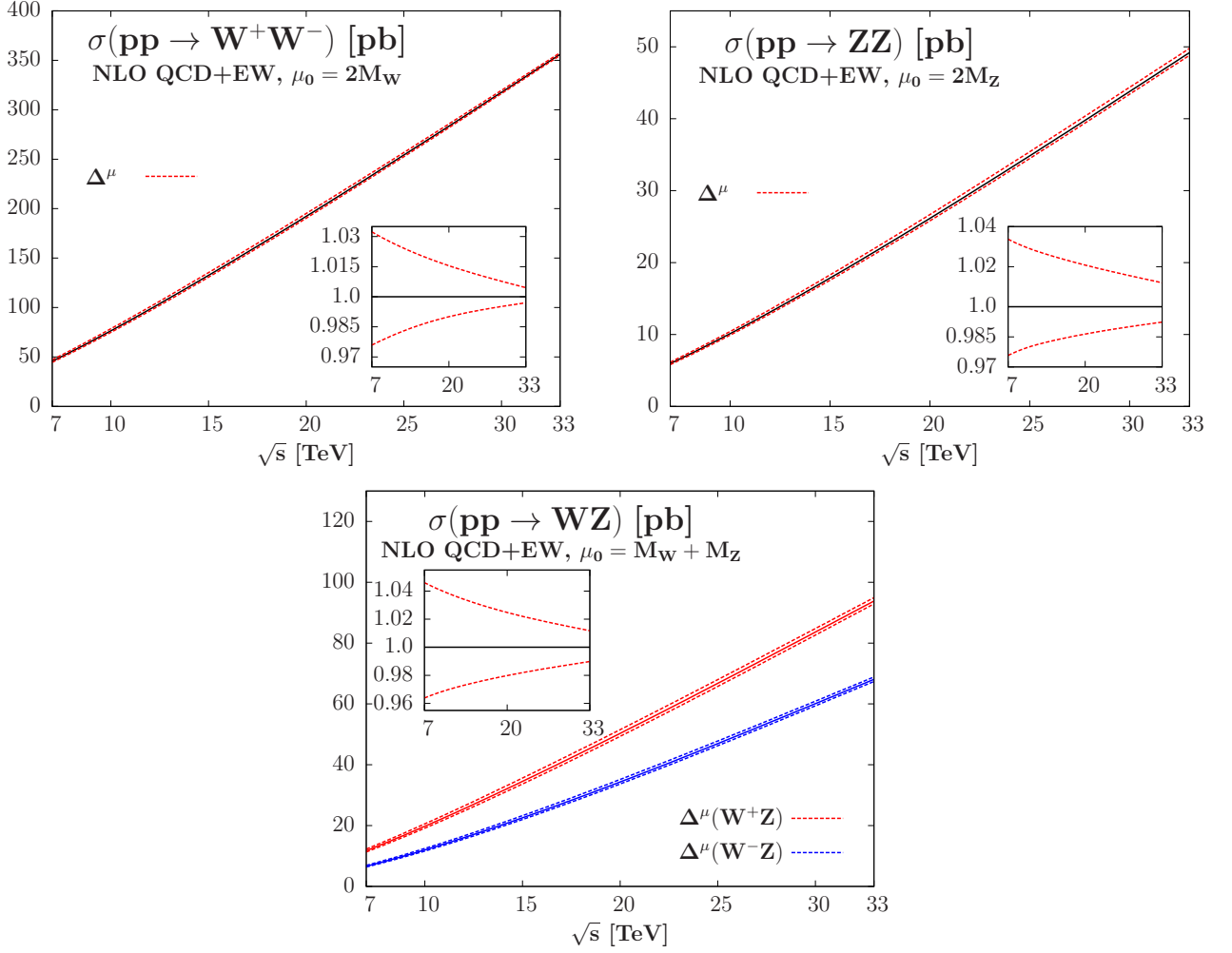


Figure 20: Scale uncertainty for a scale variation in the interval $\frac{1}{2}\mu_0 \leq \mu_R = \mu_F \leq 2\mu_0$ in $\sigma(pp \rightarrow WW, ZZ, WZ)$ (in pb) at the LHC as a function of \sqrt{s} (in TeV). Upper left: WW cross section. Upper right: ZZ cross section. Lower: W^+Z and W^-Z cross sections. In the inserts the relative deviation from the central cross section obtained with $\mu_R = \mu_F = \mu_0 = M_{V_1} + M_{V_2}$ is shown, $V_i = W/Z$.

first one calculates (in a perturbative framework) the partonic cross section, then the result is convoluted with the non-perturbative parton distribution functions that are the probability distribution of extracting from the proton a given parton with a momentum fraction x of the initial proton. The PDFs are fitted quantities on experimental data sets and that leads to uncertainties in the theoretical calculation. There are many different sets on the market, depending on the choice of the parametrization, the set of input parameters used, the running of the parameters, etc. One way to quantify the pure theoretical uncertainties induced by these differences is to compare the predictions obtained with the various sets, such as MSTW2008 [62], CT10 [65], ABM11 [66], HERA [67] or NNPDF 2.3 [68]. Each PDF collaboration uses different experimental and theoretical assumptions, e.g. which data to be used to build the fit, heavy-flavor scheme, running of the parameters, etc. In addition, the value of the strong coupling constant $\alpha_s(M_Z^2)$ is also fitted together with the PDF sets. The MSTW Collaboration central value is $\alpha_s(M_Z^2) = 0.12018$ at NLO, while CT10 uses $\alpha_s(M_Z^2) = 0.118$, the ABM11 central value

is $\alpha_s(M_Z^2) = 0.11797$, HERA 1.5 uses $\alpha_s(M_Z^2) = 0.1176$ and the NNPDF 2.3 central value is $\alpha_s(M_Z^2) = 0.117$. We display in Fig. 21 the total cross sections for WW , ZZ and WZ production at the LHC when using these different PDF sets. Only best-fit sets are used and this exemplifies the sizable differences between the various predictions, up to +6% in WW and ZZ channel from ABM11 PDF set with respect to MSTW PDF set and even more in W^+Z with a +8% increase. The lower values are generally obtained with NNPDF PDF set which deviates between -2% and -4% from the prediction obtained with MSTW PDF set. CT10 predictions tend to be closer to MSTW predictions except for the case of W^-Z production where CT10 prediction is lower than MSTW prediction by 2% to 4%. The numbers are also given in Tables 1, 2, 3 and 4. Note that we have only displayed numbers for NLO QCD cross sections as the impact of EW corrections is limited and cancel out in our scheme when comparing with MSTW predictions.

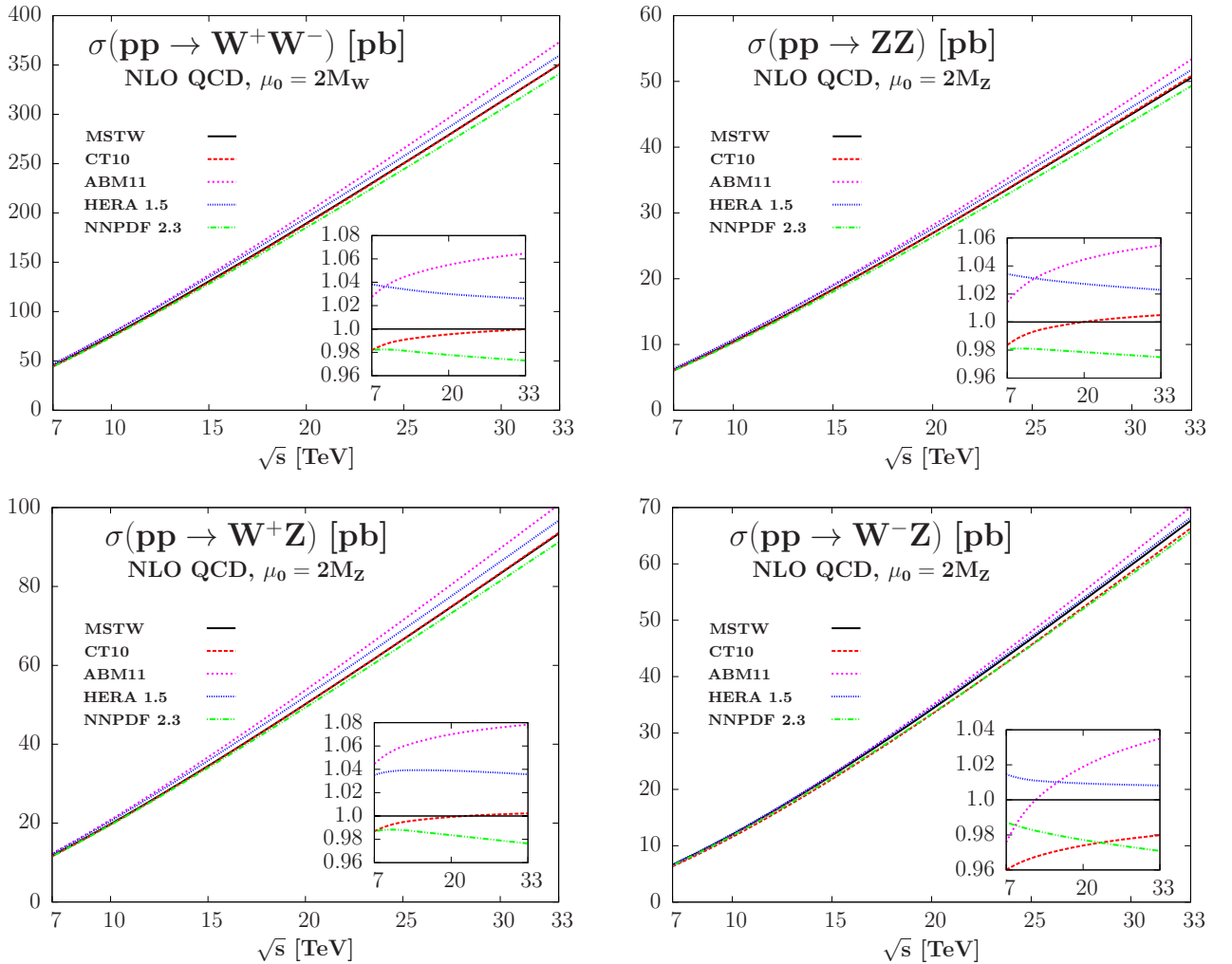


Figure 21: Total cross sections (in pb) as a function of the c.m. energy (in TeV) for WW (upper left), ZZ (upper right), W^+Z (lower left) and W^-Z (lower right) production channels at the LHC when using different PDF sets. In the inserts the relative deviation from the central cross section obtained with MSTW2008 PDF set is shown.

\sqrt{s} [TeV]	MSTW [pb]	CT10 [pb]	ABM11 [pb]	HERA 1.5 [pb]	NNPDF 2.3 [pb]
7	45.06	44.24	46.30	46.78	44.25
8	54.88	54.03	56.64	56.94	53.92
14	119.28	118.32	124.90	123.22	116.97
33	350.63	350.57	373.32	359.78	341.16

Table 1: The total W boson pair production cross section at NLO in QCD at the LHC (in pb) for given c.m. energies (in TeV) at the central scale $\mu_F = \mu_R = 2M_W$, when using MSTW, CT10, ABM11, HERA 1.5 and NNPDF 2.3 PDF sets.

\sqrt{s} [TeV]	MSTW [pb]	CT10 [pb]	ABM11 [pb]	HERA 1.5 [pb]	NNPDF 2.3 [pb]
7	6.13	6.03	6.22	6.34	6.01
8	7.52	7.42	7.66	7.77	7.37
14	16.73	16.66	17.33	17.23	16.39
33	50.61	50.86	53.37	51.77	49.34

Table 2: Same as Table 1 but for ZZ case at the central scale $\mu_F = \mu_R = 2M_Z$.

\sqrt{s} [TeV]	MSTW [pb]	CT10 [pb]	ABM11 [pb]	HERA 1.5 [pb]	NNPDF 2.3 [pb]
7	11.75	11.59	12.27	12.16	11.59
8	14.34	14.19	15.04	14.87	14.17
14	31.44	31.32	33.42	32.68	31.03
33	93.38	93.60	100.70	96.71	91.18

Table 3: Same as Table 1 but for W^+Z case at the central scale $\mu_F = \mu_R = M_W + M_Z$.

\sqrt{s} [TeV]	MSTW [pb]	CT10 [pb]	ABM11 [pb]	HERA 1.5 [pb]	NNPDF 2.3 [pb]
7	6.60	6.34	6.44	6.70	6.52
8	8.31	7.99	8.16	8.42	8.19
14	20.26	19.64	20.38	20.47	19.88
33	67.67	66.31	70.04	68.23	65.70

Table 4: Same as Table 1 but for W^-Z case at the central scale $\mu_F = \mu_R = M_W + M_Z$.

Besides the differences between the sets, there are experimental uncertainties associated with the experimental data used to build the fit. MSTW, CT10, HERA and ABM Collaborations use the Hessian method to build additional sets next to the best-fit PDF to account for the experimental uncertainties in the data used to build the distribution functions. Additional $2N_{\text{PDF}}$ sets are built from the $\pm 1\sigma$ variation around the minimal χ^2 of all N_{PDF} parameters

that enter the fit, the tolerance interval depending on the collaboration. Note that the NNPDF Collaboration uses an alternative method to build the additional sets based on Monte-Carlo replicas. Using the 90% CL error PDF sets provided by the MSTW Collaboration a PDF error of about $\sim +3.5\%/ - 3.0\%$ is obtained for $\sqrt{s} = 7$ TeV in the WW and ZZ channels, slightly more in the WZ channels with an error of $\sim \pm 4.0\%$. The uncertainty reduces down to $\sim +3.0\%/ - 2.5\%$ ($\sim \pm 3\%$) at $\sqrt{s} = 33$ TeV in the WW and ZZ channels (WZ channels).

On top of the pure PDF uncertainty, the value of the strong coupling constant α_s induces also an uncertainty in the theoretical prediction of the hadronic cross sections. Even if this will not be a dominant effect in diboson production as the three different channels are purely electroweak processes at leading order, the impact of the uncertainty on $\alpha_s(M_Z^2)$ is not negligible as the QCD corrections are large. The MSTW Collaboration provides additional PDF sets such that the combined PDF+ α_s uncertainties can be evaluated in a consistent way taking into account the correlation between the PDF and α_s [69]. The fitted value of $\alpha_s(M_Z^2)$ is then:

$$\begin{aligned}\alpha_s^{\text{NLO}}(M_Z^2) &= 0.12018_{-0.00151}^{+0.00122}(\text{at } 68\% \text{ CL}) \text{ or }_{-0.00386}^{+0.00317}(\text{at } 90\% \text{ CL}) , \\ \alpha_s^{\text{NNLO}}(M_Z^2) &= 0.11707_{-0.00135}^{+0.00141}(\text{at } 68\% \text{ CL}) \text{ or }_{-0.00342}^{+0.00337}(\text{at } 90\% \text{ CL}) ,\end{aligned}\quad (29)$$

and with the 90% CL error PDF sets we obtain a PDF+ α_s error that is slightly larger than the pure PDF uncertainty in the three different diboson channels: $\sim +4.2\%/ - 3.5\%$ in the WW and ZZ channels, $\sim +4.5\%/ - 4.0\%$ in the WZ channels, all at $\sqrt{s} = 7$ TeV. It then reduces down to $\sim \pm 4.0\%$ in the three diboson channels at $\sqrt{s} = 33$ TeV. Note that W^+Z and W^-Z channels have similar uncertainties, the difference being up to $\sim 0.5\%$ at 7 TeV in the lower deviation.

As discussed in Ref. [70] in the case of Higgs pair production, a theoretical uncertainty on α_s could be considered, stemming from scale variation or ambiguities in the heavy flavor scheme definition. The MSTW Collaboration estimates this uncertainty for α_s to be $\Delta^{\text{th}}\alpha_s(M_Z^2) = \pm 0.003$ at NLO and $\Delta^{\text{th}}\alpha_s(M_Z^2) = \pm 0.002$ at NNLO [69]. However, this uncertainty is already included in the scale uncertainty on the input data sets included in the global fit of the PDF and therefore has already been accounted for by the PDF+ α_s error. We will not consider it separately and our final PDF+ α_s uncertainty will be the MSTW2008 PDF+ α_s uncertainty, exemplified in Fig. 22. It can be noted that in general it accounts for the differences between the various PDF sets seen in Fig. 21.

4.3 Total uncertainty and comparison with experimental cross sections

Before comparing with experimental data on diboson production, we combine the errors to obtain our prediction for the total theoretical uncertainty. Following the LHC Higgs Cross Section Working Group [71], we do not use a quadratic addition that would be too optimistic and simply add linearly scale and PDF+ α_s uncertainties. We do not use the alternative combination presented in Ref. [72] in the case of Higgs production, the scale uncertainty being too limited to have sizable effects on the calculating of the PDF+ α_s uncertainty. We obtain sizable uncertainties in the different diboson production channels, ranging from $\sim +8\%/ - 6\%$ at 7 TeV in WW and ZZ channels, $\sim +9\%/ - 8\%$ in WZ channels, down to $\sim +4 - 5\%/ - 4\%$ at 33 TeV in WW and ZZ channels, $\sim \pm 5\%$ in WZ channels. This is displayed in Fig. 23 and also detailed in Tables 5, 6 and 7.

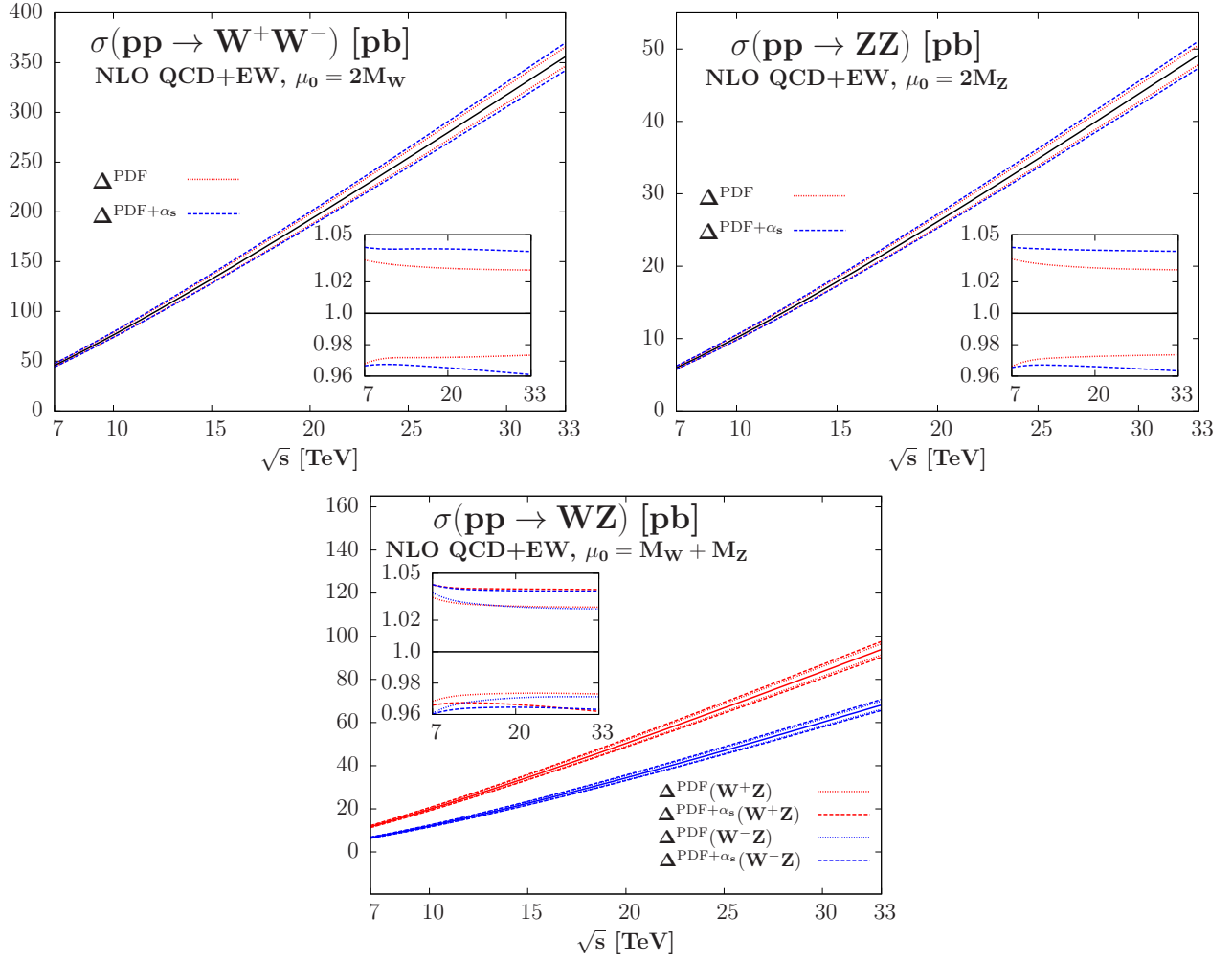


Figure 22: PDF and PDF+ α_s uncertainties using MSTW2008 PDF set in $\sigma(pp \rightarrow WW, ZZ, WZ)$ (in pb) at the LHC as a function of the c.m. energy \sqrt{s} (in TeV). Upper left: WW cross section. Upper right: ZZ cross section. Lower: W^+Z and W^-Z cross sections. In the inserts the relative deviation from the central cross section is shown.

\sqrt{s} [TeV]	σ_{WW}^{NLO} [pb]	Scale [%]		PDF [%]		PDF+ α_s [%]		Total [%]	
7	45.65	+3.2	-2.4	+3.4	-3.2	+4.2	-3.3	+7.4	-5.8
8	55.61	+3.1	-2.3	+3.3	-3.1	+4.2	-3.3	+7.2	-5.6
14	120.96	+2.2	-1.5	+3.0	-2.8	+4.1	-3.3	+6.3	-4.8
33	356.02	+0.5	-0.3	+2.8	-2.7	+3.9	-3.9	+4.4	-4.2

Table 5: The total W boson pair production cross section at NLO in QCD+EW at the LHC (in pb) for given c.m. energies (in TeV) at the central scale $\mu_F = \mu_R = 2M_W$. The corresponding deviations due to the theoretical uncertainties from the various sources discussed are shown as well as the total uncertainty when all errors are added linearly.

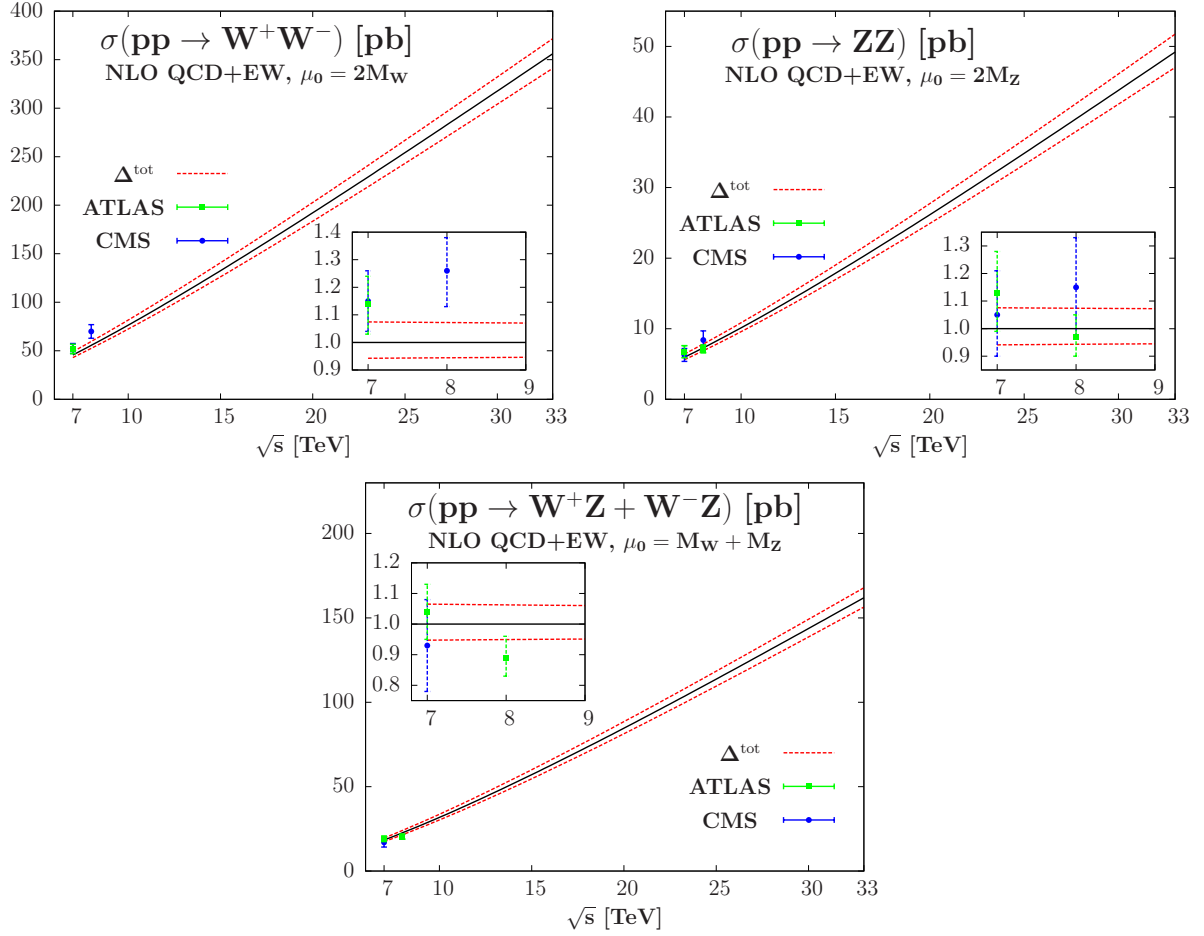


Figure 23: The NLO QCD+EW total cross section (black/full, in pb) of the processes $pp \rightarrow WW$ (upper left), $pp \rightarrow ZZ$ (upper right) and $pp \rightarrow W^+Z + W^-Z$ (lower) at the LHC as a function of the c.m. energy \sqrt{s} (in TeV) including the total theoretical uncertainty (red/dashed) as discussed in the text. The insert shows the relative deviation from the central cross sections, and the experimental data points are also displayed on the main figures.

\sqrt{s} [TeV]	σ_{ZZ}^{NLO} [pb]	Scale [%]		PDF [%]		PDF+ α_s [%]		Total [%]	
7	5.95	+3.4	-2.4	+3.5	-3.4	+4.2	-3.5	+7.6	-5.9
8	7.30	+3.2	-2.3	+3.4	-3.2	+4.2	-3.4	+7.4	-5.7
14	16.24	+2.6	-1.7	+3.0	-2.8	+4.1	-3.3	+6.6	-5.0
33	49.20	+1.2	-0.8	+2.8	-2.6	+3.9	-3.7	+5.1	-4.4

Table 6: Same as Table 5 but for ZZ case at the central scale $\mu_F = \mu_R = 2M_Z$.

We are now ready to compare with experimental results given by the ATLAS and CMS Collaborations. The latest state-of-the-art total cross section measurements at the LHC use a luminosity in the ATLAS experiment of 4.6 fb^{-1} for the WW , ZZ and WZ measurements at 7 TeV [6, 8, 73], 13 fb^{-1} for the WZ measurement at 8 TeV [74] and $20.3 \pm 0.6 \text{ fb}^{-1}$ for

\sqrt{s} [TeV]	$\sigma_{W^+Z}^{\text{NLO}}$ [pb]	Scale [%]		PDF [%]		PDF+ α_s [%]		Total [%]	
7	11.73	+4.6	-3.6	+3.5	-3.2	+4.3	-3.4	+8.9	-7.0
8	14.33	+4.4	-3.4	+3.3	-3.0	+4.2	-3.3	+8.6	-6.8
14	31.49	+3.3	-2.6	+3.0	-2.7	+4.0	-3.3	+7.3	-5.9
33	93.84	+1.2	-1.0	+2.8	-2.7	+4.0	-3.8	+5.1	-4.8

\sqrt{s} [TeV]	$\sigma_{W^-Z}^{\text{NLO}}$ [pb]	Scale [%]		PDF [%]		PDF+ α_s [%]		Total [%]	
7	6.61	+4.6	-3.6	+3.7	-3.9	+4.3	-4.0	+8.9	-7.6
8	8.32	+4.4	-3.4	+3.6	-3.7	+4.2	-3.9	+8.6	-7.3
14	20.33	+3.3	-2.6	+3.0	-3.1	+3.9	-3.6	+7.3	-6.2
33	68.09	+1.2	-1.0	+2.7	-2.9	+3.9	-3.7	+5.0	-4.7

Table 7: Same as Table 5 but for W^+Z and W^-Z cases at the central scale $\mu_F = \mu_R = M_W + M_Z$.

the ZZ measurement at 8 TeV [75]; the CMS experiment uses a luminosity of 1.1 fb^{-1} for the WZ measurement at 7 TeV [76], 3.5 fb^{-1} for the WW measurement at 8 TeV [77], 4.92 fb^{-1} for the WW measurement at 7 TeV [78], 5 fb^{-1} for the ZZ measurement at 7 TeV [11] and 5.3 fb^{-1} for the ZZ measurement at 8 TeV [77]. The experimental results are summarized

	ATLAS total cross section [pb]	CMS total cross section [pb]
WW 7 TeV	$51.9 \pm 2.0(\text{stat}) \pm 3.9(\text{syst}) \pm 2.0(\text{lumi})$	$52.4 \pm 2.0(\text{stat}) \pm 4.5(\text{syst}) \pm 1.2(\text{lumi})$
WW 8 TeV		$69.9 \pm 2.8(\text{stat}) \pm 5.6(\text{syst}) \pm 3.1(\text{lumi})$
ZZ 7 TeV	$6.7 \pm 0.7(\text{stat})_{-0.3}^{+0.4}(\text{syst}) \pm 0.3(\text{lumi})$	$6.24_{-0.80}^{+0.86}(\text{stat})_{-0.32}^{+0.41}(\text{syst}) \pm 0.14(\text{lumi})$
ZZ 8 TeV	$7.1_{-0.4}^{+0.5}(\text{stat}) \pm 0.3(\text{syst}) \pm 0.2(\text{lumi})$	$8.4 \pm 1.0(\text{stat}) \pm 0.7(\text{syst}) \pm 0.4(\text{lumi})$
WZ 7 TeV	$19.0_{-1.3}^{+1.4}(\text{stat}) \pm 0.9(\text{syst}) \pm 0.4(\text{lumi})$	$17.0 \pm 2.4(\text{stat}) \pm 1.1(\text{syst}) \pm 1.0(\text{lumi})$
WZ 8 TeV	$20.3_{-0.7}^{+0.8}(\text{stat})_{-1.1}^{+1.2}(\text{syst})_{-0.6}^{+0.7}(\text{lumi})$	

Table 8: Total cross sections measured by ATLAS and CMS experiments at the LHC in WW , ZZ and WZ channels (in pb). The latter is the sum of W^+Z and W^-Z channels. The references for these experimental results can be found in the text where the luminosity used is given.

in Table 8 and the associated references are given above with the luminosity used to measure each cross section. When comparing with our theoretical predictions, the experimental errors are summed in quadrature to obtain the final experimental uncertainty. In the case of WZ production ATLAS and CMS Collaborations give their results on the sum of W^+Z and W^-Z channels. We then add our theoretical predictions together and add in quadrature the associated uncertainties as we have treated separately the two channels. This then gives the following results:

- *WW channel*: we have at 7 TeV $\sigma_{WW}^{\text{ATLAS}} = 51.9 \pm 4.8 \text{ pb}$ and $\sigma_{WW}^{\text{CMS}} = 52.4 \pm 5.1 \text{ pb}$, giving 1.1σ and 1.2σ agreements respectively with our theoretical prediction $\sigma_{WW}^{\text{th}} = 45.7_{-2.6}^{+3.4} \text{ pb}$. At

8 TeV, we have $\sigma_{WW}^{\text{CMS}} = 69.9 \pm 7.0$ pb, giving a 1.8σ agreement with our theoretical prediction $\sigma_{WW}^{\text{th}} = 55.6_{-3.1}^{+4.0}$ pb.

- *ZZ channel:* we have at 7 TeV $\sigma_{ZZ}^{\text{ATLAS}} = 6.7_{-0.8}^{+0.9}$ pb and $\sigma_{ZZ}^{\text{CMS}} = 6.24_{-0.87}^{+0.96}$ pb, giving 0.8σ and 0.3σ agreements respectively with our theoretical prediction $\sigma_{ZZ}^{\text{th}} = 5.95_{-0.35}^{+0.45}$ pb. At 8 TeV, we have $\sigma_{ZZ}^{\text{ATLAS}} = 7.1_{-0.5}^{+0.6}$ pb and $\sigma_{ZZ}^{\text{CMS}} = 8.4 \pm 1.3$ pb, giving 0.3σ and 0.8σ agreements respectively with our theoretical prediction $\sigma_{ZZ}^{\text{th}} = 7.3_{-0.4}^{+0.5}$ pb.
- *WZ channel:* we have at 7 TeV $\sigma_{WZ}^{\text{ATLAS}} = 19.0_{-1.6}^{+1.7}$ pb and $\sigma_{WZ}^{\text{CMS}} = 17.0 \pm 2.8$ pb, giving 0.3σ and 0.4σ agreements respectively with our theoretical prediction $\sigma_{WZ}^{\text{th}} = 18.3_{-1.0}^{+1.2}$ pb. At 8 TeV, we have $\sigma_{WZ}^{\text{ATLAS}} = 20.3_{-1.4}^{+1.6}$ pb, giving a 1.2σ agreement with our theoretical prediction $\sigma_{WZ}^{\text{th}} = 22.7_{-1.1}^{+1.4}$ pb.

We obtain an overall good agreement with the experimental results, in particular in the ZZ and WZ channels with less than one standard deviation difference between theory and experiment. This can also be seen in Fig. 23 where the experimental points together with their uncertainty bands are displayed on top of our theoretical curves. The highest deviation is seen in the WW channel in particular at 8 TeV, where the experimental measurement is 1.8σ higher than the theoretical prediction.

Given the size of the gluon fusion contribution, which is formally a NNLO contribution and that one could expect being the dominant contribution because of the large gluon PDF, we estimate the size of the missing NNLO contributions in WW production to be of the same order, namely 2% on top of the full NLO result. We also assume that this will reduce the scale uncertainty down to 1% at 8 TeV which gives a 5% total uncertainty. When comparing to the CMS result, the deviation we get is 1.7σ . This means that, we think, a full NNLO calculation cannot account for this deviation. Note that after having written this, the new paper [22] appeared and its conclusion supports our estimation.

5 Conclusion

We have studied in this paper the full NLO predictions for massive gauge boson pair production at the LHC, including both QCD and EW corrections. The latter have been calculated using both mass regularization and dimensional regularization schemes, including for the first time the photon-quark induced processes, and our results are in perfect agreement with each other. Furthermore, our results without the photon-quark induced processes are similar to the results of Refs. [27–29], obtained with a different scale choice. In Section 3 we have presented a study of the differential distributions and we have analyzed the hierarchy that is observed in the size of the gluon-quark induced and photon-quark induced corrections between ZZ , WW and WZ channels. Thanks to analytical leading-logarithmic approximations we have provided the first comprehensive explanation of this hierarchy, essentially due to the non-abelian gauge structure of the SM, different coupling strengths and PDF effects. We have found that the photon-quark induced corrections are negligible in the ZZ channel, but play an important role in the EW corrections of WW and WZ channels, compensating or even overcompensating the Sudakov virtual effects. This is because, even though the photon PDF is suppressed, a new enhancement mechanism with a t -channel exchange of a gauge boson occurs in the hard processes for WW and WZ channels.

In Section 4 we have studied the total cross sections and the theoretical uncertainties that affect the predictions. The parametric errors on the W and Z masses have been found negligible, and the sum of the scale uncertainty and the PDF+ α_s uncertainty are limited to less than $\pm 9\%$ in all channels at all c.m. energy ranging from 7 to 33 TeV. We have also studied the spread in the predictions using different PDF sets and have found a $\simeq 4\%$ deviation at maximum with respect to the default MSTW2008 prediction in all channels. The comparison with ATLAS and CMS experimental results has also been done and we have found excellent agreement in the ZZ and WZ channels at 7 and 8 TeV. The agreement in the WW channel is at the 1σ level at 7 TeV and at the 1.8σ level at 8 TeV when comparing to the CMS result. We have estimated that even if a full NNLO result were available this level of agreement would not significantly differ. This experimental enhancement has triggered some analyses in terms of new physics to explain it, for example supersymmetric explanations with charginos effects [79] or stops contributions [80].

Acknowledgments: We thank Dao Thi Nhung and Dieter Zeppenfeld for fruitful discussions. This work is supported by the Deutsche Forschungsgemeinschaft via the Sonderforschungsbereich/Transregio SFB/TR-9 Computational Particle Physics.

A Analytical calculation of $d\sigma(u\gamma \rightarrow W^+Zd)$ in leading-logarithmic approximation

We present in this appendix the details of the calculation, in leading-logarithmic approximation, of the EW photon-quark induced process $u\gamma \rightarrow W^+Zd$ in the high p_T^Z regime. This process is chosen as an example because it is the most complicated one including all important features. The following notations, already introduced in Section 3, will be used for the coupling of gauge bosons to quarks,

$$c_{L,q} = \frac{1}{\sin\theta_W \cos\theta_W} (I_3^q - Q_q \sin^2\theta_W), \quad a_W = \frac{1}{\sqrt{2} \sin\theta_W}. \quad (30)$$

One has also the following relations between the couplings,

$$c_{L,u} - c_{L,d} = \cot\theta_W, \quad Q_u - Q_d = 1, \quad Q_u = a_W^2 - \cot\theta_W c_{L,u}, \quad Q_d = -a_W^2 - \cot\theta_W c_{L,d}. \quad (31)$$

The leading-logarithmic contribution for the process $u\gamma \rightarrow W^+Zd$ in the high p_T^Z limit is calculated by considering soft W^+ radiation. Thus we display in Fig. 24 the Feynman diagrams for this process with a classification in four categories depending on the $2 \rightarrow 2$ production process of the hard Z boson. In Fig. 24a one has the soft radiation of the W^+ boson from the initial up quark line, in Fig. 24b there is a soft radiation from the final down quark line, in Fig. 24c the W^+ radiated off the final Z line and in Fig. 24d the soft radiation is from the initial photon line.

Before calculating the process, we note that the amplitudes only make use of left-handed quarks as a W boson is produced. In any $2 \rightarrow 2$ process involving two gauge bosons we also note that the only helicity amplitudes surviving at high energy are those where the two gauge

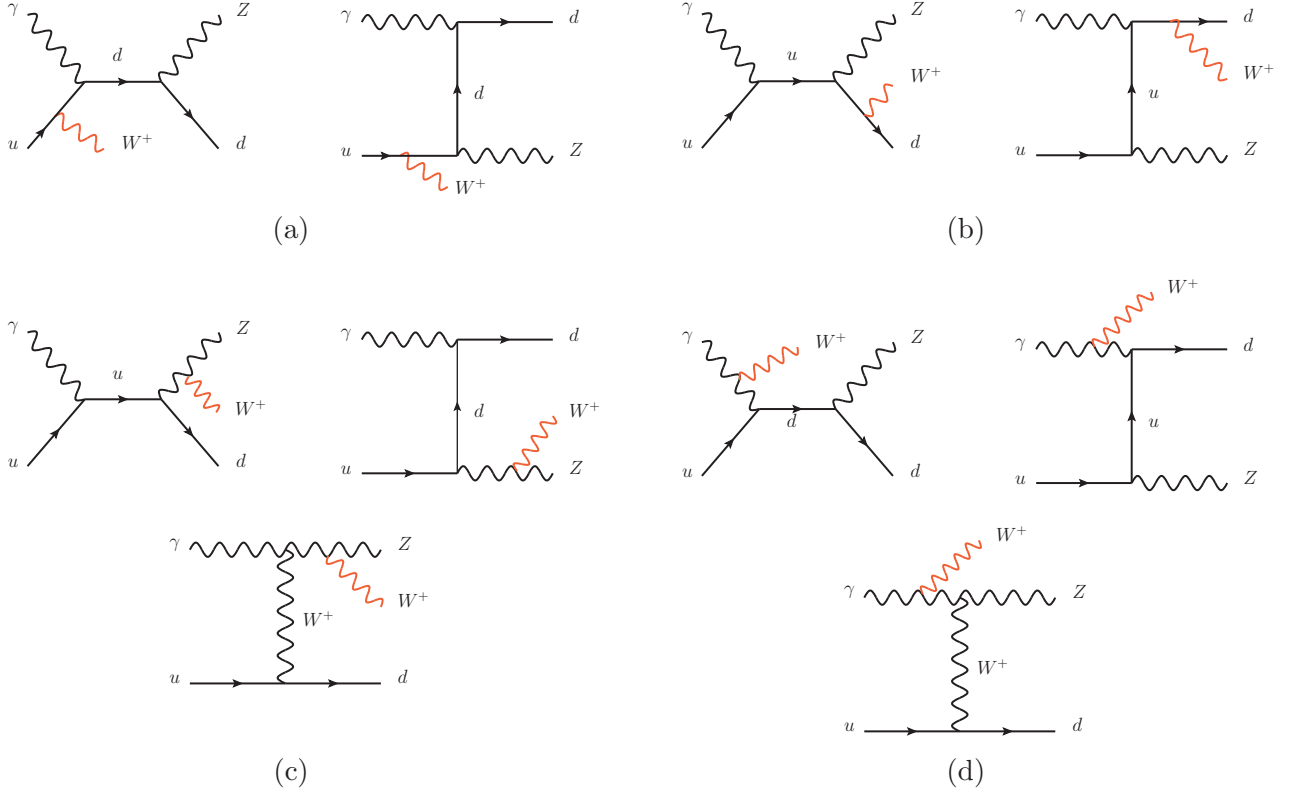


Figure 24: Diagrams for $u\gamma \rightarrow W^+Zd$ production cross section in the case of the differential p_T^Z distribution. The soft W^+ is displayed in red and the diagrams are classified in four categories depending on the $2 \rightarrow 2$ hard Z subprocess: a) is for $d\gamma \rightarrow Zd$, b) is for $u\gamma \rightarrow Zu$, c) is for $u\gamma \rightarrow W^+d$ and d) is for $uW^- \rightarrow Zd$.

bosons are either both transverse or both longitudinal. This conclusion agrees with Ref. [81]. We then have the following amplitudes,

$$\begin{aligned}
 \mathcal{M}_a &= ea_W \frac{p_u \cdot \varepsilon^*(k)}{p_u \cdot k} \mathcal{A}_L^{d\gamma \rightarrow Zd}, & \mathcal{M}_b &= -ea_W \frac{p_d \cdot \varepsilon^*(k)}{p_d \cdot k} \mathcal{A}_L^{u\gamma \rightarrow Zu}, \\
 \mathcal{M}_c &= e \cot \theta_W \frac{p_Z \cdot \varepsilon^*(k)}{p_Z \cdot k} \mathcal{A}_L^{u\gamma \rightarrow W^+d}, & \mathcal{M}_d &= -e \frac{p_\gamma \cdot \varepsilon^*(k)}{p_\gamma \cdot k} \mathcal{A}_{LT}^{uW^- \rightarrow Zd},
 \end{aligned} \tag{32}$$

where k stands for the momentum of the soft W^+ boson, the subscript L means that all quarks are left-handed and T means that all gauge bosons are transverse. As we work in the high p_T regime we have $p^2 \rightarrow 0$ for any of the external particle (in the leading-logarithmic approximation). This means that only the interference terms between the various amplitudes \mathcal{M}_i survive, then killing the longitudinal term in \mathcal{M}_d as we always have a photon involved in the interference between \mathcal{M}_d and the other amplitudes. This explains why we have already discarded this longitudinal term in Eq. (32) above, the other amplitudes being always transverse at high energy as they involve a photon. This argument that only transverse gauge bosons can contribute to the leading-logarithmic results also holds for the ZZ and W^+W^- cases and is crucial for obtaining simple results.

When integrating over the W^+ boson phase-space we use the following soft approximation,

$$\int_{M_W}^E \frac{d^3k}{(2\pi)^3 2\omega_k} \frac{2p_i p_j}{(p_i \cdot k)(p_j \cdot k)} = \frac{1}{8\pi^2} \log^2 \left(\frac{p_T^2}{M_W^2} \right) \quad \text{in the limit } M_W^2 \ll p_T^2 \simeq E^2. \quad (33)$$

When squaring the sum of the amplitudes in Eq. (32) and using Eq. (33) one has

$$\begin{aligned} |\bar{\mathcal{A}}^{u\gamma \rightarrow W^+ Z d}|^2 &= \frac{1}{2} \left[a_W^2 \Re \left(\mathcal{A}_L^{d\gamma \rightarrow Z d} \mathcal{A}_L^{u\gamma \rightarrow Z u^*} \right) + \cot \theta_W \Re \left(\mathcal{A}_L^{u\gamma \rightarrow W^+ d} \mathcal{A}_{LT}^{uW^- \rightarrow Z d^*} \right) + \right. \\ &\quad a_W \Re \left(\mathcal{A}_L^{d\gamma \rightarrow Z d^*} \left(-\cot \theta_W \mathcal{A}_L^{u\gamma \rightarrow W^+ d} + \mathcal{A}_{LT}^{uW^- \rightarrow Z d} \right) \right) - \\ &\quad \left. a_W \Re \left(\mathcal{A}_L^{u\gamma \rightarrow Z u^*} \left(-\cot \theta_W \mathcal{A}_L^{u\gamma \rightarrow W^+ d} + \mathcal{A}_{LT}^{uW^- \rightarrow Z d} \right) \right) \right] \frac{\alpha}{2\pi} \log^2 \left[\frac{(p_T^Z)^2}{M_W^2} \right], \quad (34) \end{aligned}$$

where it is implicitly assumed that the sum over color is done in the real part of the amplitude products. The quarks are taken left-handed only in the $2 \rightarrow 2$ subprocesses which implies the extra one-half factor coming from the spin average in the unpolarized $2 \rightarrow 3$ process. The gauge bosons are all transverse but yet unpolarized and their spin average is implicitly assumed in the above expression.

The key point is now to relate the two amplitudes $\mathcal{A}_L^{u\gamma \rightarrow W^+ d}$ and $\mathcal{A}_{LT}^{uW^- \rightarrow Z d}$ to the amplitude $\mathcal{A}_L^{u\gamma \rightarrow Z u}$. By using only transverse gauge bosons one can link the amplitude $\mathcal{A}_{3L}^{u\gamma \rightarrow W^+ d}$ displayed by the third diagram of Fig. 24c to the amplitude $\mathcal{A}_{3LT}^{uW^- \rightarrow Z d}$ displayed by the third diagram of Fig. 24d for the $2 \rightarrow 2$ hard subprocess: $\mathcal{A}_{3LT}^{uW^- \rightarrow Z d} = \cot \theta_W \mathcal{A}_{3L}^{u\gamma \rightarrow W^+ d}$. This gives

$$\begin{aligned} \mathcal{A}_L^{u\gamma \rightarrow W^+ d} &= \frac{a_W}{c_{L,u}} \mathcal{A}_{1L}^{u\gamma \rightarrow Z u} + \frac{Q_d}{Q_u} \frac{a_W}{c_{L,u}} \mathcal{A}_{2L}^{u\gamma \rightarrow Z u} + \mathcal{A}_{3L}^{u\gamma \rightarrow W^+ d}, \\ \mathcal{A}_{LT}^{uW^- \rightarrow Z d} &= -\frac{a_W}{Q_u} \frac{c_{L,d}}{c_{L,u}} \mathcal{A}_{1L}^{u\gamma \rightarrow Z u} - \frac{a_W}{Q_u} \mathcal{A}_{2L}^{u\gamma \rightarrow Z u} + \cot \theta_W \mathcal{A}_{3L}^{u\gamma \rightarrow W^+ d}, \quad (35) \end{aligned}$$

from which one obtains the following equation, with the use of Eq. (31),

$$\cot \theta_W \mathcal{A}_L^{u\gamma \rightarrow W^+ d} - \mathcal{A}_{LT}^{uW^- \rightarrow Z d} = a_W a_u \mathcal{A}_L^{u\gamma \rightarrow Z u}, \quad (36)$$

with $a_u = 1 - (Q_d c_{L,d}) / (Q_u c_{L,u})$ as defined in Eq. (18). This (which is the same as Eq. (19)) is the master equation to express the differential cross section in a simple form. We also use the following equation

$$\mathcal{A}_L^{d\gamma \rightarrow Z d} = \frac{Q_d}{Q_u} \frac{c_{L,d}}{c_{L,u}} \mathcal{A}_L^{u\gamma \rightarrow Z u} \quad (37)$$

to replace the $d\gamma \rightarrow Z d$ subprocess by the $u\gamma \rightarrow Z u$ subprocess. Using Eq. (36) two times one can link not only the amplitudes together but also the squared amplitudes, giving

$$2 \cot \theta_W \Re \left(\mathcal{A}_L^{u\gamma \rightarrow W^+ d} \mathcal{A}_{LT}^{uW^- \rightarrow Z d^*} \right) = \cot^2 \theta_W \left| \mathcal{A}_L^{u\gamma \rightarrow W^+ d} \right|^2 + \left| \mathcal{A}_{LT}^{uW^- \rightarrow Z d} \right|^2 - a_W^2 a_u^2 \left| \mathcal{A}_L^{u\gamma \rightarrow Z u} \right|^2. \quad (38)$$

The final result is obtained when inserting Eq. (36) and Eq. (38) into Eq. (34), leading to

$$d\sigma^{u\gamma \rightarrow W^+ Z d} = \left[\frac{a_W^2}{2} \left(1 - a_u + \frac{a_u^2}{2} \right) d\sigma_L^{u\gamma \rightarrow Z u} + \frac{\cot^2 \theta_W}{4} d\sigma_L^{u\gamma \rightarrow W^+ d} + \frac{1}{4} d\sigma_{LT}^{uW^- \rightarrow Z d} \right] \frac{\alpha}{2\pi} \log^2 \left[\frac{(p_T^Z)^2}{M_W^2} \right], \quad (39)$$

where the photon PDF has to be used, at the hadronic level, for the initial W^- . This ends our proof of Eq. (17) where the result for $d\gamma \rightarrow W^- Z u$ process is also given. Similar results for $q\gamma \rightarrow ZZq$, $q\gamma \rightarrow W^\pm Zq'$ and $q\gamma \rightarrow W^+W^-q$, obtained using the above explained method, can be found in Section 3.2, Section 3.3 and Section 3.4, respectively. The result for the QCD gluon-quark induced process $ug \rightarrow W^+ Z d$ can be derived from Eq. (39) using the following rules: $\gamma \rightarrow g$, $Q_q \rightarrow 1$, $d\sigma_L^{u\gamma \rightarrow W^+d} \rightarrow d\sigma_L^{ug \rightarrow W^+d}$ and $d\sigma_{LT}^{uW^- \rightarrow Zd} \rightarrow 0$.

References

- [1] ATLAS Collaboration, G. Aad *et al.*, (2013), arXiv:1302.2929.
- [2] ATLAS Collaboration, G. Aad *et al.*, Phys.Rev. **D85**, 032009 (2012), arXiv:1111.2690.
- [3] CMS Collaboration, S. Chatrchyan *et al.*, JHEP **10**, 132 (2011), arXiv:1107.4789.
- [4] CMS Collaboration, S. Chatrchyan *et al.*, JHEP **06**, 126 (2012), arXiv:1204.1643.
- [5] ATLAS Collaboration, G. Aad *et al.*, Phys.Lett. **B712**, 289 (2012), arXiv:1203.6232.
- [6] ATLAS Collaboration, G. Aad *et al.*, (2012), arXiv:1210.2979.
- [7] ATLAS Collaboration, G. Aad *et al.*, Phys.Rev.Lett. **108**, 041804 (2012), arXiv:1110.5016.
- [8] ATLAS Collaboration, G. Aad *et al.*, JHEP **1303**, 128 (2013), arXiv:1211.6096.
- [9] ATLAS Collaboration, G. Aad *et al.*, Phys.Lett. **B709**, 341 (2012), arXiv:1111.5570.
- [10] ATLAS Collaboration, G. Aad *et al.*, Phys.Lett. **B717**, 49 (2012), arXiv:1205.2531.
- [11] CMS Collaboration, S. Chatrchyan *et al.*, JHEP **1301**, 063 (2013), arXiv:1211.4890.
- [12] LHC Higgs Cross Section Working Group, S. Dittmaier *et al.*, (2012), arXiv:1201.3084.
- [13] J. Ohnemus, Phys.Rev. **D44**, 3477 (1991).
- [14] S. Frixione, P. Nason, and G. Ridolfi, Nucl.Phys. **B383**, 3 (1992).
- [15] S. Frixione, Nucl.Phys. **B410**, 280 (1993).
- [16] L. J. Dixon, Z. Kunszt, and A. Signer, Nucl.Phys. **B531**, 3 (1998), hep-ph/9803250.
- [17] J. M. Campbell and R. K. Ellis, Phys.Rev. **D60**, 113006 (1999), hep-ph/9905386.
- [18] J. M. Campbell, R. K. Ellis, and C. Williams, JHEP **1107**, 018 (2011), arXiv:1105.0020.
- [19] J. Ohnemus, Phys.Rev. **D50**, 1931 (1994), hep-ph/9403331.
- [20] T. Melia, P. Nason, R. Rontsch, and G. Zanderighi, JHEP **1111**, 078 (2011), arXiv:1107.5051.
- [21] F. Campanario and S. Sapeta, Phys.Lett. **B718**, 100 (2012), arXiv:1209.4595.
- [22] S. Dawson, I. M. Lewis, and M. Zeng, (2013), arXiv:1307.3249.
- [23] J. Kuhn, F. Metzler, A. Penin, and S. Uccirati, JHEP **1106**, 143 (2011), arXiv:1101.2563.
- [24] E. Accomando, A. Denner, and S. Pozzorini, Phys.Rev. **D65**, 073003 (2002), hep-ph/0110114.
- [25] E. Accomando, A. Denner, and A. Kaiser, Nucl.Phys. **B706**, 325 (2005), hep-ph/0409247.

- [26] E. Accomando, A. Denner, and C. Meier, *Eur.Phys.J.* **C47**, 125 (2006), hep-ph/0509234.
- [27] A. Bierweiler, T. Kasprzik, H. Kühn, and S. Uccirati, *JHEP* **1211**, 093 (2012), arXiv:1208.3147.
- [28] A. Bierweiler, T. Kasprzik, and J. H. Kuhn, (2012), arXiv:1208.3404.
- [29] A. Bierweiler, T. Kasprzik, and J. H. Kühn, (2013), arXiv:1305.5402.
- [30] D. A. Dicus, C. Kao, and W. Repko, *Phys.Rev.* **D36**, 1570 (1987).
- [31] E. N. Glover and J. van der Bij, *Phys.Lett.* **B219**, 488 (1989).
- [32] E. N. Glover and J. van der Bij, *Nucl.Phys.* **B321**, 561 (1989).
- [33] T. Binoth, M. Ciccolini, N. Kauer, and M. Krämer, *JHEP* **0503**, 065 (2005), hep-ph/0503094.
- [34] T. Binoth, M. Ciccolini, N. Kauer, and M. Krämer, *JHEP* **0612**, 046 (2006), hep-ph/0611170.
- [35] T. Binoth, N. Kauer, and P. Mertsch, p. 142 (2008), arXiv:0807.0024.
- [36] G. 't Hooft and M. Veltman, *Nucl.Phys.* **B44**, 189 (1972).
- [37] S. Catani and M. Seymour, *Nucl.Phys.* **B485**, 291 (1997), hep-ph/9605323.
- [38] M. S. Chanowitz, M. Furman, and I. Hinchliffe, *Nucl.Phys.* **B159**, 225 (1979).
- [39] K. Aoki, Z. Hioki, M. Konuma, R. Kawabe, and T. Muta, *Prog.Theor.Phys.Suppl.* **73**, 1 (1982).
- [40] A. Denner, S. Dittmaier, and R. Schuster, *Nucl.Phys.* **B452**, 80 (1995), hep-ph/9503442.
- [41] A. Sirlin, *Phys.Rev.* **D22**, 971 (1980).
- [42] A. Denner, *Fortsch.Phys.* **41**, 307 (1993), arXiv:0709.1075.
- [43] S. Dittmaier, *Nucl.Phys.* **B565**, 69 (2000), hep-ph/9904440.
- [44] NNPDF Collaboration, S. Carrazza, (2013), arXiv:1305.4179.
- [45] A. Martin, R. Roberts, W. Stirling, and R. Thorne, *Eur.Phys.J.* **C39**, 155 (2005), hep-ph/0411040.
- [46] S. Dittmaier and M. Huber, *JHEP* **1001**, 060 (2010), arXiv:0911.2329.
- [47] A. Bredenstein, A. Denner, S. Dittmaier, and S. Pozzorini, *JHEP* **0808**, 108 (2008), arXiv:0807.1248.
- [48] T. Hahn, *Comput.Phys.Commun.* **140**, 418 (2001).

- [49] T. Hahn and M. Perez-Victoria, *Comput. Phys. Commun.* **118**, 153 (1999).
- [50] H. Murayama, I. Watanabe, and K. Hagiwara, KEK Report No. KEK-91-11, 1992 (unpublished).
- [51] J. Alwall *et al.*, *JHEP* **0709**, 028 (2007).
- [52] G. van Oldenborgh, *Comput.Phys.Comm.* **66**, 1 (1991).
- [53] G. Passarino and M. Veltman, *Nucl.Phys.* **B160**, 151 (1979).
- [54] G. 't Hooft and M. Veltman, *Nucl.Phys.* **B153**, 365 (1979).
- [55] S. Dittmaier, *Nucl.Phys.* **B675**, 447 (2003).
- [56] D. T. Nhung and L. D. Ninh, *Comput.Phys.Comm.* **180**, 2258 (2009), arXiv:0902.0325.
- [57] A. Denner and S. Dittmaier, *Nucl.Phys.* **B844**, 199 (2011).
- [58] U. Baur, S. Keller, and D. Wackerroth, *Phys.Rev.* **D59**, 013002 (1998), hep-ph/9807417.
- [59] Particle Data Group, J. Beringer *et al.*, *Phys.Rev.* **D86**, 010001 (2012).
- [60] ATLAS Collaboration, G. Aad *et al.*, *Phys.Lett.* **B716**, 1 (2012), arXiv:1207.7214.
- [61] CMS Collaboration, S. Chatrchyan *et al.*, *Phys.Lett.* **B716**, 30 (2012), arXiv:1207.7235.
- [62] A. Martin, W. Stirling, R. Thorne, and G. Watt, *Eur.Phys.J.* **C63**, 189 (2009), arXiv:0901.0002.
- [63] D. T. Nhung, L. D. Ninh, and M. M. Weber, (2013), arXiv:1307.7403.
- [64] I. W. Stewart and F. J. Tackmann, *Phys.Rev.* **D85**, 034011 (2012), arXiv:1107.2117.
- [65] H.-L. Lai *et al.*, *Phys.Rev.* **D82**, 074024 (2010), arXiv:1007.2241.
- [66] S. Alekhin, J. Blumlein, and S. Moch, *Phys.Rev.* **D86**, 054009 (2012), arXiv:1202.2281.
- [67] H1 Collaboration, ZEUS Collaboration, V. Radescu, (2011), arXiv:1107.4193.
- [68] NNPDF Collaboration, R. D. Ball *et al.*, *Nucl.Phys.* **B855**, 153 (2012), arXiv:1107.2652.
- [69] A. Martin, W. Stirling, R. Thorne, and G. Watt, *Eur.Phys.J.* **C64**, 653 (2009), arXiv:0905.3531.
- [70] J. Baglio *et al.*, *JHEP* **1304**, 151 (2013), arXiv:1212.5581.
- [71] LHC Higgs Cross Section Working Group, S. Dittmaier *et al.*, (2011), arXiv:1101.0593.
- [72] J. Baglio and A. Djouadi, *JHEP* **1010**, 064 (2010), arXiv:1003.4266.
- [73] ATLAS Collaboration, G. Aad *et al.*, *Eur.Phys.J.* **C72**, 2173 (2012), arXiv:1208.1390.

- [74] ATLAS Collaboration, CERN Report No. ATLAS-CONF-2013-021, 2013 (unpublished).
- [75] ATLAS Collaboration, CERN Report No. ATLAS-CONF-2013-020, 2013 (unpublished).
- [76] CMS Collaboration, CERN Report No. CMS-PAS-EWK-11-010, 2011 (unpublished).
- [77] CMS Collaboration, S. Chatrchyan *et al.*, Phys.Lett. **B721**, 190 (2013), arXiv:1301.4698.
- [78] CMS Collaboration, CERN Report No. CMS-PAS-SMP-12-005, 2012 (unpublished).
- [79] D. Curtin, P. Jaiswal, and P. Meade, Phys.Rev. **D87**, 031701 (2013), arXiv:1206.6888.
- [80] K. Rolbiecki and K. Sakurai, (2013), arXiv:1303.5696.
- [81] U. Baur, T. Han, and J. Ohnemus, Phys.Rev.Lett. **72**, 3941 (1994), hep-ph/9403248.